

**Real-time monitoring of plasma synthesis of functional materials by high power impulse magnetron sputtering and other PVD processes: towards a physics-constrained digital twin**

EHIASARIAN, Arutiun <<http://orcid.org/0000-0001-6080-3946>>, ARUNACHALAM SUGUMARAN, Arunprabhu <<http://orcid.org/0000-0002-5087-4297>>, HOVSEPIAN, Papken <<http://orcid.org/0000-0002-1047-0407>>, DAVIES, Clive and HATTO, Peter

Available from Sheffield Hallam University Research Archive (SHURA) at:

<https://shura.shu.ac.uk/31024/>

---

This document is the Published Version [VoR]

**Citation:**

EHIASARIAN, Arutiun, ARUNACHALAM SUGUMARAN, Arunprabhu, HOVSEPIAN, Papken, DAVIES, Clive and HATTO, Peter (2022). Real-time monitoring of plasma synthesis of functional materials by high power impulse magnetron sputtering and other PVD processes: towards a physics-constrained digital twin. *Journal of Physics D: Applied Physics*, 56 (3): 035302. [Article]

---

**Copyright and re-use policy**

See <http://shura.shu.ac.uk/information.html>

PAPER • OPEN ACCESS

## Real-time monitoring of plasma synthesis of functional materials by high power impulse magnetron sputtering and other PVD processes: towards a physics-constrained digital twin

To cite this article: A P Ehiasarian *et al* 2022 *J. Phys. D: Appl. Phys.* **56** 035302

View the [article online](#) for updates and enhancements.

You may also like

- [An ionization region model for high-power impulse magnetron sputtering discharges](#)  
M A Raadu, I Axnäs, J T Gudmundsson *et al.*
- [Optimizing the deposition rate and ionized flux fraction by tuning the pulse length in high power impulse magnetron sputtering](#)  
Martin Rudolph, Nils Brenning, Michael A. Raadu *et al.*
- [Plasma dynamic in chromium and titanium HIPIMS discharges](#)  
Alena Vetushka and Arutiun P Ehiasarian

### ECS Toyota Young Investigator Fellowship



For young professionals and scholars pursuing research in batteries, fuel cells and hydrogen, and future sustainable technologies.

At least one \$50,000 fellowship is available annually.  
More than \$1.4 million awarded since 2015!



Application deadline: January 31, 2023

**Learn more. Apply today!**

# Real-time monitoring of plasma synthesis of functional materials by high power impulse magnetron sputtering and other PVD processes: towards a physics-constrained digital twin

A P Ehasarian<sup>1,\*</sup> , A A Sugumaran<sup>1</sup>, P Eh Hovsepiyan<sup>1</sup>, C Davies<sup>2</sup> and P Hatto<sup>2</sup>

<sup>1</sup> National HIPIMS Technology Centre, Sheffield Hallam University, Howard St, Sheffield S1 1WB, United Kingdom

<sup>2</sup> Ionbond UK Ltd, No 1 Industrial Estate, Consett, Co Durham DH8 6TS, United Kingdom

E-mail: [a.ehasarian@shu.ac.uk](mailto:a.ehasarian@shu.ac.uk)

Received 5 July 2022, revised 8 November 2022

Accepted for publication 14 November 2022

Published 20 December 2022



CrossMark

## Abstract

Plasma synthesis of thin films by physical vapour deposition (PVD) enables the creation of materials that drive significant innovations in modern life. High value manufacturing demand for tighter quality control and better resource utilisation can be met by a digital twin capable of modelling the deposition process in real time. Optical emission spectroscopy (OES) was combined with process parameters to monitor all stages of both high power impulse magnetron sputtering and conventional magnetron sputtering processes to provide a robust method of determining process repeatability and a reliable means of process control for quality assurance purposes. Strategies and physics-based models for the *in-situ* real-time monitoring of coating thickness, composition, crystallographic and morphological development for a CrAlYN/CrN nanoscale multilayer film were developed. Equivalents to the ion-to-neutral ratio and metal-to-nitrogen ratios at the substrates were derived from readily available parameters including the optical emission intensities of Cr I, N<sub>2</sub> (C–B) and Ar I lines in combination with the plasma diffusivity coefficient obtained from the ratio of substrate and cathode current densities. These optically-derived equivalent parameters identified the deposition flux conditions which trigger the switch of dominant crystallographic texture from (111) to (220) observed in XRD pole figures and the development of coating morphology from faceted to dense for a range of magnetron magnetic field configurations. OES-based strategies were developed to monitor the progress of chamber evacuation, substrate cleaning and preventative chamber wall cleaning to support process optimisation and equipment utilisation. The work paves the way to implementation of machine learning protocols for monitoring and control of these and other processing activities, including coatings development and the use of alternative

\* Author to whom any correspondence should be addressed.



Original content from this work may be used under the terms of the [Creative Commons Attribution 4.0 licence](https://creativecommons.org/licenses/by/4.0/). Any further distribution of this work must maintain attribution to the author(s) and the title of the work, journal citation and DOI.

deposition techniques. The work provides essential elements for the creation of a digital twin of the PVD process to both monitor and predict process outcomes such as film thickness, texture and morphology in real time.

Keywords: high power impulse magnetron sputtering, optical emission spectroscopy, thin film microstructure, digital twin, physical vapour deposition

(Some figures may appear in colour only in the online journal)

## 1. Introduction

The plasma synthesis of thin films by physical vapour deposition (PVD) has enabled the creation of many materials that have been a driving force behind significant innovations in modern life [1]. However, the full potential of the technology is currently untapped having penetrated a fraction of the available high value manufacturing applications because industrial processes lack sufficient design predictability and struggle to achieve sufficient reproducibility and controllability. As quality control is typically offline, errors are discovered after the deposition process leading to reworking or losses. Existing process control solutions are commonly based on narrowly specialised feedback loops such as those embedded in the plasma generators [2] and plasma optical emission (OE) monitoring systems coupled with gas flow control [3] and designed to maintain their output constant regardless of the deposition environment. This approach fails to monitor and respond to the actual environment within the chamber created by the plasma generation conditions, magnetic field setup, and the chemical state of the substrates, cathodes, anode and chamber wall. There is little work on a holistic approach to PVD coating growth with the ability to account for all steps of the deposition process by specifying appropriate strategies for monitoring the actual environment, simulating and predicting the coating properties and controlling the process deposition environment.

Digital twins are a potent way of improving quality control and resource utilisation and are a powerful tool for process design due to the intrinsic flexibility of design of data collection and simulation, which allows them to take into account the complete deposition process and the environment in which it is deployed. Digital twins are most impactful when operating at sufficiently low latency (in real time). They deploy fast collection of data from the process and use it as an input to a reduced-order simulation thus creating a real-time (low latency) virtual representation of the system. Crucially, they provide real-time control commands to the deposition system. Currently a digital twin of a PVD process is lacking essential building blocks such as accessible process monitoring data in real time (physical twin) and a real-time simulation approach.

For example, existing methods for PVD coating adhesion assurance rely on a product-specific in-chamber ‘conditioning’ procedure but have no means of ensuring that surfaces are actually sufficiently clean before coating deposition begins. Approaches for monitoring substrate etching are well developed in semiconductor manufacturing but are not

typically applicable to PVD. These utilise machine vision and spectral filters to spatially resolve etch rates, relying on the ability to image the entire substrate surface [4]. Self-excited electron resonance spectroscopy [5] uses a probe at the chamber wall to determine plasma density by analysing harmonics in the plasma sheath of RF discharges. Optical emission spectroscopy (OES) is used to monitor the species at the reactor wall and in the plasma volume and determine chamber cleanliness or to raise an alarm and perform a predetermined set of actions if the spectrum deviates from a standard [6]. A virtual metrology approach combining OES and electrical ‘plasma information’ parameters has been used with machine learning algorithms to predict etch rates for wafers [7–10]. Infrared spectroscopy [11] and laser induced fluorescence are used to detect chamber condition or etching end-point but are costly or not applicable to reflective coatings typical of PVD.

Similarly, existing methods for coating thickness assurance control source power and deposition time, followed by a post-coating measurement to determine if the required thickness has been achieved. Coating texture has a marked impact on coating performance hence it is important to be able to select and control it to ensure reproducible performance. Theoretical analysis shows that the crystallographic texture of a CrN film is correlated to the relative fluxes of metal and dissociated (atomic) nitrogen arriving at the surface ( $j_{Me/N}^S$ ) [12, 13]. Cr adatoms have lower diffusivity on (111) than (110) and (100) surfaces due to their surface energies being related as  $\gamma_{111} < \gamma_{110} < \gamma_{100}$  [14] and is naturally trapped on these nitrogen rich surfaces thus promoting growth of these textures. High fluxes of atomic nitrogen (low  $j_{Me/N}^S$ ) promote the formation of CrN dimers and trap metal on (200) and (220) surfaces which are metal rich compared to (111), thus promoting those textures.

The ion-to-neutral ratio ( $j_{i/n}^S$ ) and the metal-to-dissociated nitrogen ratio ( $j_{Me/N}^S$ ) near the substrate are known [15, 16] to play an important role in determining adatom mobility and surface reactions which together set the balance between diffusion limited and reaction limited modes of film growth which promote high or low-surface energy surfaces. Calculating these ratios requires plasma diagnostics data on plasma density and neutral flux commonly extracted using Langmuir probes, plasma chemistry using plasma-sampling energy-resolved mass spectroscopy, deposition monitors and retarding field analysers with a quartz crystal microbalance detector. Moreover, they require long campaigns of acquisition and analysis, which are incompatible with the real time control agenda. All these diagnostics tools are invasive and

often difficult to implement in a practical process where substrates should not be shadowed and may be moving in three-fold rotation. Even if these tools were available, in the majority of cases they are not compatible with the real deposition environment and are rarely used at the same time as the deposition itself.

Simulation of the plasma PVD process can revolve around physics-based models of plasma-surface interactions as well as *ab initio* modelling of plasma generation and film growth. Physics-based models of coating growth are grounded on structure zone models that take into account temperature [17], pressure [17, 18], bombardment energy [19] and effect of impurities [15] as well as studies of the impact of ionisation on microstructure and texture [20]. These models are limited in their ability to determine the combined effects of multiple parameters in the environment on coating growth. Conventional *ab initio* modelling of the plasma generation process or coating growth process is very precise, and based on Particle-in-Cell Monte Carlo [12, 21] and density functional theory [13, 22] approaches and multi-scale models [23] which are able to follow the full timescale of the process but are not real time.

Monitoring of process inputs can provide rich information but there is insufficient knowledge in selecting appropriate sensors and process data and reliably predicting the growth of films and their properties in real time.

We report on the results from a recently completed joint work between Ionbond UK Limited and Sheffield Hallam University, which utilises OES in combination with external process parameters to monitor and potentially control, in real-time, all stages of the high power impulse magnetron sputtering (HIPIMS) process, including: system evacuation and vacuum quality; the progress and end-point detection of plasma cleaning, strongly related to coating adhesion; coating thickness, coating crystallographic texture and grain morphology; as well as providing the necessary data for condition monitoring and maintenance of coating equipment. To monitor crystallographic texture and grain morphology, we introduce two optically-derived ratios ( $\mathcal{J}_{Me/N}^S$  and  $\mathcal{J}_{i/n}^S$ ) that are representative of the metal-to-dissociated nitrogen ratio ( $j_{Me/N}^S$ ) and the ion-to-neutral ratio ( $j_{i/n}^S$ ) in the deposition flux and are available in real time.

The work constitutes the essential elements of a digital twin. To achieve near real-time/low latency operation, it proposes physics-based reduced-order models which can be solved rapidly latency and which rely on process data which is both readily accessible from non-invasive sensors and available in real time. The work combines a number of signals and information on the setup to extract in real time fundamental physical quantities such as ion-to-neutral ratio, metal-to-nitrogen ratios and contamination levels which govern film growth, influencing grain morphology and texture. In this, the work goes beyond both conventional monitoring and plasma diagnostics. Process monitoring is confined to rudimentary signals, often single rather than in combination, and is focused on maintaining a particular parameter constant rather than providing information on the coating itself.

By providing low-latency information, the work also goes beyond plasma diagnostics, which is often invasive, requiring the installation of probes at the position of the substrate and dedicated measurement campaigns which are typically not compatible with concomitant thin film deposition. Hence, the work paves the way to the creation of a digital twin, which is able to continuously receive information and update a digital replica to reflect the current state of the process and use it to control the process. The work paves the way to big data collection and implementation of machine learning protocols for monitoring and control of these and other processing activities, including coatings development and the use of alternative deposition techniques.

It is strongly expected that these results will be transferable to other PVD and related processing technologies, including arc evaporation and PACVD, to provide the technical means for enhanced, real-time quality assurance and traceability of PVD and related processes and coatings. This will give design engineers, especially those engaged in high value manufacturing, the confidence to specify such coatings at an early stage in the component design process in the knowledge that those using the technology are operating in the same quality and traceability space as other tier 1 suppliers.

## 2. Experimental

### 2.1. Study methodology

Initially, strategies were developed by Sheffield Hallam University for the real-time monitoring and control of coating thickness, coating composition, including coating texture, and coating adhesion by monitoring the intensity of specific OE lines from different plasma species, cathode current and substrate current. CrAlYN/CrN nanoscale multilayer coatings based on previous research [24–27] and deposited in an in-house Hauzer Techno Coating 1000/4 coating system were selected as a model process. The deposition system is schematically shown in figure 1. It has four magnetron sources, with target dimensions of 200 × 600 mm, two of which are operated in HIPIMS mode and two in conventional direct current magnetron sputtering (DCMS) mode.

The strategies were used in Ionbond UK Limited to record, analyse and interpret OE spectra from production coating cycles to provide production relevant data identifying meaningful OE lines and intensity changes as indicators of and triggers for: completion of pump-down; substrate sputter cleaning/conditioning; chamber condition monitoring; together with preliminary validation of the strategies developed at Sheffield Hallam University. Production cycles monitored were for a Cr-based coating deposited in Ionbond's Hauzer 1500 max 424 system, with four magnetron sources with target dimensions of 170 × 1680 mm. The coating was chosen as it was subject to a high production rate allowing data from a larger number of cycles to be recorded. The composition, crystallographic texture, grain morphology and thickness, of CrAlYN/CrN nanoscale multilayer coatings were characterised for films deposited at Sheffield Hallam University.

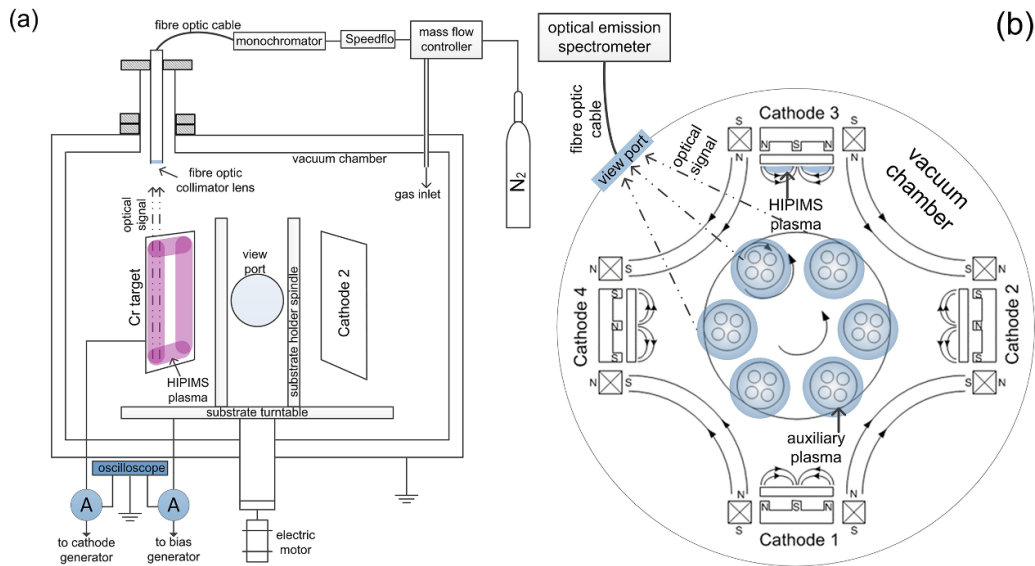


**Figure 1.** Vertical cross sections of the deposition system at Sheffield Hallam University showing (a) light collection and current measurements during the deposition step and (b) light collection during the etching step.

## 2.2. Process sequence

The PVD process comprised the stages of pump-down, target cleaning, substrate surface plasma pre-treatment, and coating. In a typical process the substrates were subjected to a three-fold rotation.

The substrates used at Sheffield Hallam University, were 304 stainless steel (SS) disks with dimensions diam.  $30 \times 4$  mm and plates with dimensions  $25 \times 25 \times 0.8$  mm and silicon. At Ionbond the substrates comprised customer supplied SS speaker grills of various dimensions.

Substrate pre-treatment (etching) was performed at the conclusion of pump-down and target cleaning to remove surface contamination from substrates prior to coating deposition. The substrates were biased to a potential of a few hundred volts and immersed in a plasma discharge which was created in the chamber. At the university facilities a HIPIMS discharge was used for this purpose allowing the substrates to be bombarded with Ar and Cr ions [26]. The HIPIMS glow discharge was operated in an Argon atmosphere by applying a pulse voltage with a peak potential of  $-1000$  V to the cathode using a HIPIMS generator type HighPulse 4008 (Trumpf Hüttinger Electronics Sp. z O.O., Poland). The ion mixture was accelerated towards the substrate by applying a DC substrate bias voltage of  $-1000$  V using a dedicated HIPIMS bias supply (Trumpf Hüttinger Electronics Sp. z O.O., Poland) capable of maintaining a stable voltage for peak currents of up to 300 A.

The CrAl<sub>Y</sub>N/Cr<sub>N</sub> multilayer coating [24–27] was deposited in a reactive Ar + N<sub>2</sub> atmosphere at 400 °C using two Cr, one Cr<sub>0.4</sub>Al<sub>0.6</sub> and one Cr<sub>0.38</sub>Al<sub>0.58</sub>Y<sub>0.04</sub> target. Three different unbalancing coil currents: 0, 4 and 7 A were used for the coating deposition [28]. The substrate bias voltage was kept constant at  $-65$  V for all processes. OE line of Cr I neutral excited atoms (resonant transition from an upper excitation energy of 2.9 eV) at 425.4 nm was used to control these processes

following a previously established procedure [29]. A multi-channel feedback control system for high-speed adjustment of a reactive gas (Speedflo by Gencoa Ltd) was operated in ‘sensor’ mode, i.e. the N<sub>2</sub> gas flow was adjusted in order to keep the observed emission intensity of Cr I from the CrAlY cathode at a particular set point value throughout the deposition process. To choose the sensor set point value to deposit the coatings, the hysteresis in the observed sensor signal for Cr I (excited neutral) emission while varying the nitrogen flow from 0 to 300 sccm and back to 0 sccm [30] was obtained for each coil current. The optical signal gain was adjusted to obtain 95% in metallic mode and 20% in fully poisoned mode. To maintain the stoichiometry of the coatings for processes with unbalancing coil currents of 0, 4 and 7 A, the set point values were 58%, 28% and 27% respectively.

The discharge current during the deposition was measured by an oscilloscope model TPS 2024 (Tektronix) using a 1000:1 current probe type i1000S (Fluke). The substrate current during the deposition was measured by an oscilloscope model TPS 2024 (Tektronix) using a 10:1 current monitor probe type 101 (Pearson). The width of the erosion zone of the cathode (racetrack) for different unbalancing coil currents was determined from computer simulations using Finite Element Method Magnetics software [31]. The film texture of as deposited films was determined on SS 304 mirror polished unoriented substrates using x-ray diffraction pole figures obtained by an Emyrean x-ray diffractometer (Panalytical) with Co K $\alpha$  radiation (1.789 Å). The surface morphology and cross-sectional microstructure of the coatings were analysed by Scanning Electron Microscopy (FEI Nova NanoSEM 200). The stoichiometry of the coatings was studied using energy dispersive x-ray (EDX) spectroscopy (Oxford instruments) at 20 kV. Grain size was obtained from SEM plan view images at a magnification of 50 000 using ImageJ [32] to identify and count the maxima in intensity associated with the top surface

of each grain. An average grain area was calculated by dividing the area of observation by the number of maxima and the average grain diameter was calculated from the area assuming a circular shape.

### 2.3. OES equipment and monitoring

OES monitoring at Sheffield Hallam University was undertaken using a Czerny-Turner type monochromator (Triax 320—Jobin Yvon) with a resolution of 0.2 nm operated in time-averaged mode. The spectrometer was equipped with a charge coupled device (CCD) detector, which could observe a 64 nm wide portion of the spectrum with a millisecond time resolution.

During the substrate pre-treatment stage at Sheffield Hallam University, the substrates were monitored whilst undergoing three-fold rotation as in a real deposition run. To achieve this, light from the substrates was collected with a quartz optical fibre attached to one of the main glass view ports on the door of the system as shown in figure 1(b). The optical fibre was oriented in line with the SS samples and was used without additional optics in order to maximise the angle of collection.

During the coating deposition step, light was collected *in vacuo* through a quartz optical fibre attached to a quartz telescopic lens feedthrough at the top of the chamber as shown in figure 1(a). To avoid coating and reducing optical transmission, the fibre was equipped with a 10 cm long collimator tube which was placed in a 40 mm diameter vacuum tube extending 20 cm above the wall. The collimator was directed at 8° with respect to the target surface and sampled the plasma from the racetrack of the cathode directly in front of the target.

During the pumping and heating steps, monitoring was done at Ionbond on a Hauzer 1500 max industrial coating system and was based on an Optix optical gas analysis system (Gencoa Ltd). This uses a sensor inside a modified Penning gauge which is mounted on the backing line of the system and operates over a pressure range from 0.5 to  $10^{-6}$  mbar. The Optix monitors the auxiliary plasma emission created in the Penning gauge under reproducible plasma density and electron temperature conditions. As this system is principally designed for the OES analysis of gaseous components, it was supplemented with an optical assembly for viewing directly inside the vacuum chamber but using the Optix spectrum analyser, allowing detailed analysis of plasma components, including metallic species. The instrument has a resolution of approximately 0.4 nm using a CCD analyser with 2000 pixels covering a wavelength range of 200–900 nm. The control software allows the collection of spectra for up to 20 pre-selected species or full plasma spectra at an update rate of between 5 ms and 5 s, depending on the sensitivity selected. Using this equipment, spectral data was collected from a total of 172 coating cycles. To study chamber wall contamination and predict conditioning cycles, spectral monitoring was used to analyse the plasma generated in the modified Penning device attached directly to the coating chamber to monitor gaseous components during chamber evacuation and post-coating/pre-venting stages.

The emission lines used for monitoring the different stages of the process are summarised in table A1 in the appendix.

## 3. Results and discussion

Strategies for monitoring, simulation and control were developed for each of the process steps including pump-down, target cleaning, substrate surface plasma pre-treatment, and coating as well as chamber wall condition monitoring.

### 3.1. Vacuum quality assessment

During the pump-down stage of the industrial process, the auxiliary plasma produced by the Optix system emitted a spectrum comprising H I line spectra from the Balmer series and OH (A–X) molecular bands at 284 nm ( $1-0, A^2\Sigma^+ - X^2\Pi$ ) and 309.6 nm ( $0-0, A^2\Sigma^+ - X^2\Pi$ ) (see figure 2). These species are produced by a process of electron impact molecular dissociation of water vapour which produces H and OH radicals and the subsequent electron impact excitation of the H and OH to produce OE. The most relevant line was found to be the Balmer H $\beta$  I at 486.13 nm ( $n = 4 \rightarrow n' = 2$ ), which has a high oscillator strength, its intensity stayed within detectable limits throughout the process, and its position did not overlap with other species. The emission line observed here originates from an electron occupying the upper excitation state  $n = 4$ , which has decayed to the  $n' = 2$  lower state, however the decay could also proceed directly to the ground state  $n' = 1$  emitting in the deep ultraviolet beyond the detection limit of the instrument. As both of these transitions have a similar probability of occurring, the observed line is a reliable indicator of the density of hydrogen atoms in the ground state. The H $\alpha$  I line at 656.28 nm ( $n = 3 \rightarrow n' = 2$ ) is another favourable candidate possessing high oscillator strength and being free of overlap, however its high emission intensity saturated the detector of the Optix system at the start of pumping, and this continued until after the mid-stage of pumping (see figures 2 and 3). The individual rotational transitions within the OH molecular band could not be resolved by the Optix spectrometer. Figures 2(b) and (c) show that as the pumping progressed, the shape of the 284 nm band changed, and additional lines appeared adjacent to the 309 nm band indicating that both bands are overlapping with other species. As gas and contaminants in the Optix plasma are depleted, the intensity falls as well as seen by the reduced scale of figure 2(c).

Figure 3 shows that during pump-down the intensity of H $\beta$  reduces monotonically and provides an excellent correlation with the chamber environment. In contrast, the direct pressure measurement was not sufficiently sensitive to the evolution of hydrogen (figure 3). The pressure gauge signal saturated as the gauge reached its detection limit thus introducing significant inaccuracy in the indication for vacuum quality. Taking into consideration the conditions recorded for a number of standard runs, the empirically-determined criterion for the completion of a single pump-down phase was a reduction in

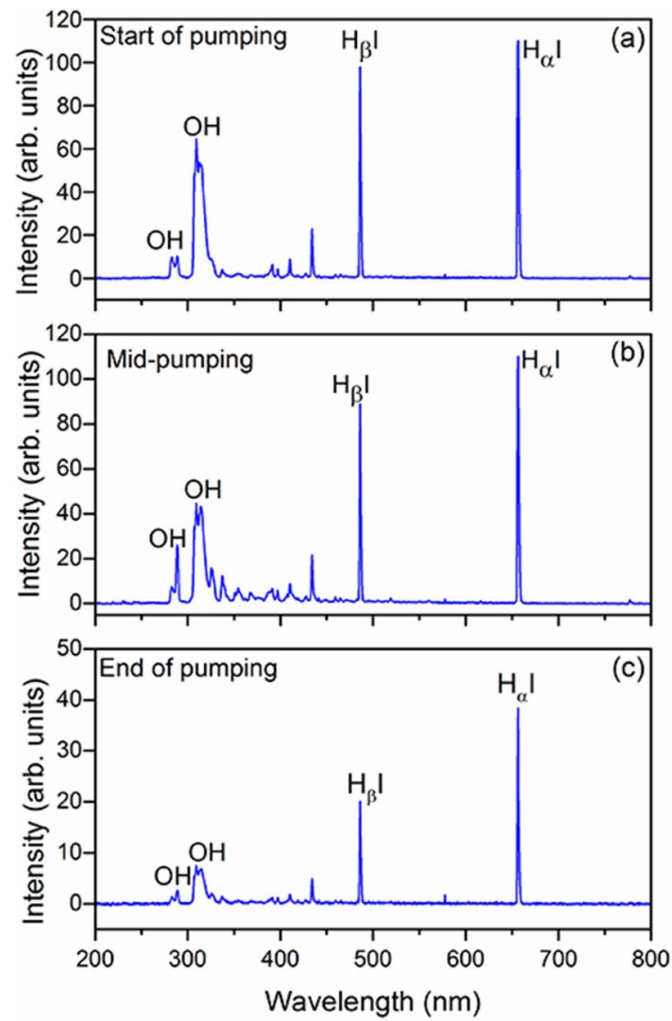


**Figure 2.** Spectrum from the auxiliary plasma in the Optix system exhibiting emission lines from H and OH at (a) ‘start’ of pumping (0.5 mbar), (b) mid-stage of pumping, and (c) end of pumping (note change in intensity scale).

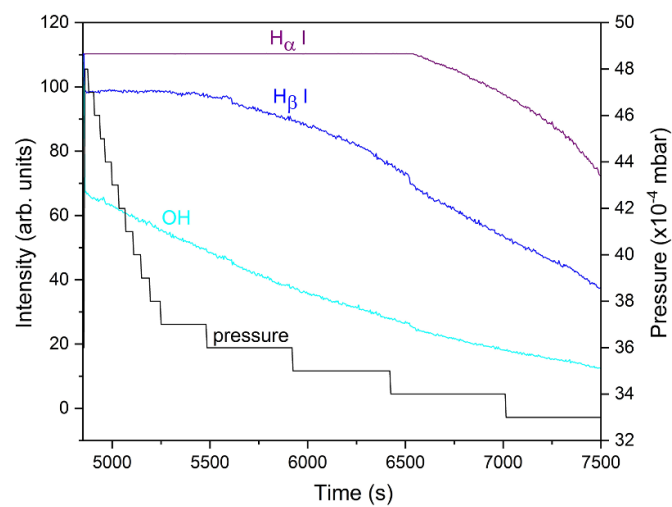


**Figure 3.** Intensity of OES signals from H $\alpha$  I, H $\beta$  I and OH and pressure reading versus time in seconds during pump-down phase, showing saturation of Optix detector by H $\alpha$  I during much of initial pump-down.

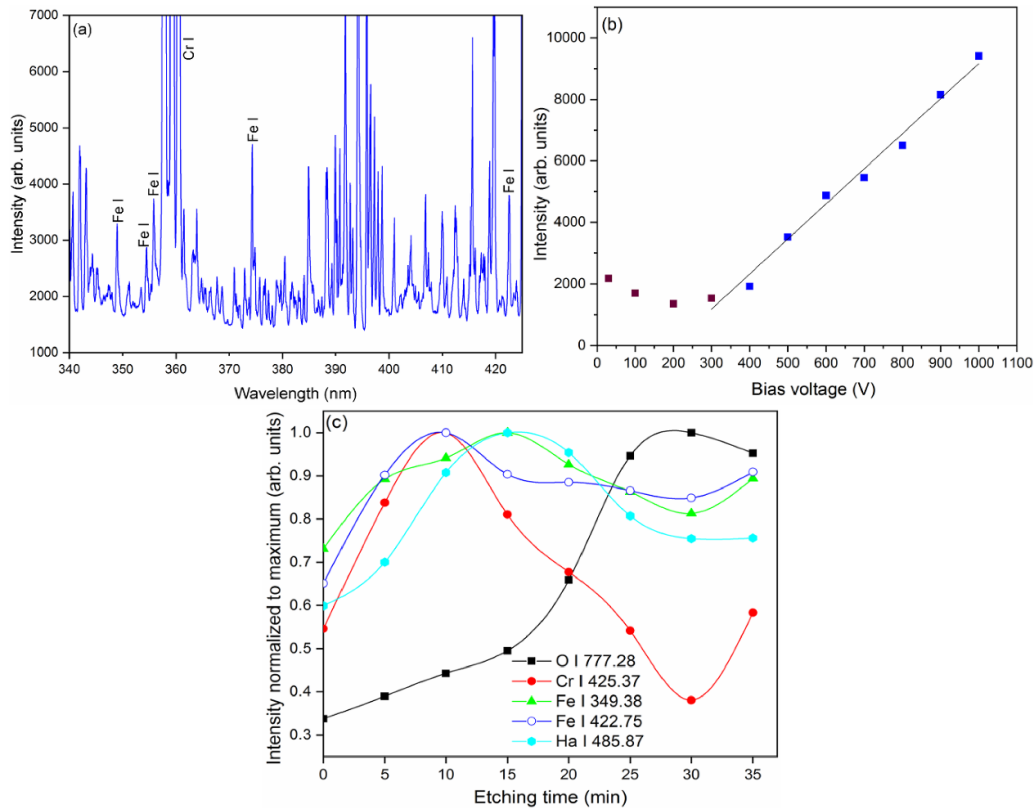


**Figure 4.** (a) Emission lines of Fe I and Cr I (neutral excited atom) observed during the substrate surface decontamination procedure and (b) Emission intensity of Fe I 354 nm as a function of substrate bias voltage during etching. Substrates were stationary and a fibre optic cable was placed *in vacuo* oriented parallel to the surface. (c) Evolution of emission intensity with time.

intensity of  $H_{\beta}$  by >85% of the peak value at start of monitoring ( $\sim 0.5$  mbar at switch-on).

### 3.2. End-point detection during substrate pretreatment

The emission intensity of various gas species observed at the beginning and end stages of the etching procedure are shown in figures 4(a)–(c) and 5(a)–(f). During etching, the substrate material is removed by sputtering along with substrate contaminants such as oxygen and hydrogen. Several emission lines for Fe I neutral excited atoms were observed and identified in the spectrum in figure 4(a). Strong emission from Cr was also detected due to reflection of light from the cathode by the fixtures and the sputtering of previously-deposited Cr from the fixture surfaces.

Increasing the bias voltage from  $-400$  to  $-1000$  V had the effect of increasing Fe I emission by a factor of 7 (figure 4(b)) due to an increasing sputter yield (0.9–1.5 for  $Ar^+$  on Fe) and substrate etching rate. This confirms that the line is associated with substrate processes and does not originate from reflected light from the cathode. For bias voltage values below  $-400$  V, there was a constant emission intensity indicating a slow etching, net deposition or an overlap with another line. Figure 4(c) shows the evolution of emission intensity of Fe I, Cr I, O I (777 nm triplet originating from  $3p(^5P_{1,2,3}) - 3s(^5S_2^o)$  transitions) and  $H_{\alpha}$  I lines over the course of an etching step. The emission lines for hydrogen could be attributed to residual

gases in the chamber. The presence of O I emission indicates the sputtering of oxide contamination from the surface of the substrate and residual gases. In the initial stages of the etching step, Fe I and Cr I intensity rises steeply compared to O I as substrates are progressively sputter-cleaned. At around 20 min, the intensities of O I and  $H_{\alpha}$  I increase due to a rise in temperature in the chamber which results in oxygen evolution from the fixtures. The additional outgassing re-contaminates the substrates, resulting in a drop in Fe I emission. At the end of the step, O I and  $H_{\alpha}$  I emissions begin to drop and Fe I rises again as the outgassing abates and the surfaces start cleaning up again.

The intensity of  $H_{\alpha}$  I neutral excited atom at the start of the process is about 25 000 counts which decreased to about 12 000 as etching progressed (figures 5(a) and (b)). Similar drops in intensity were observed for  $H_{\beta}$  I (figures 5(c) and (d)) and O I (figures 5(e) and (f)). Note that as etching is not started until pump-down is complete the problem of detector saturation by the strength of the  $H_{\alpha}$  I signal, discussed in section 3.1, is not relevant in the case of the etching process. It should also be noted that the spectra in this section and section 3.1 were taken with different spectrometers which have different saturation levels. Section 3.1 spectra are from the Optix instrument which has a saturation level of 100. This section shows spectra from the Triax 320 which has a saturation level of 65 000.

To exclude the effect of intensity reduction due to coating of the viewport, it is useful to take the ratio between  $H_{\beta}$  I and

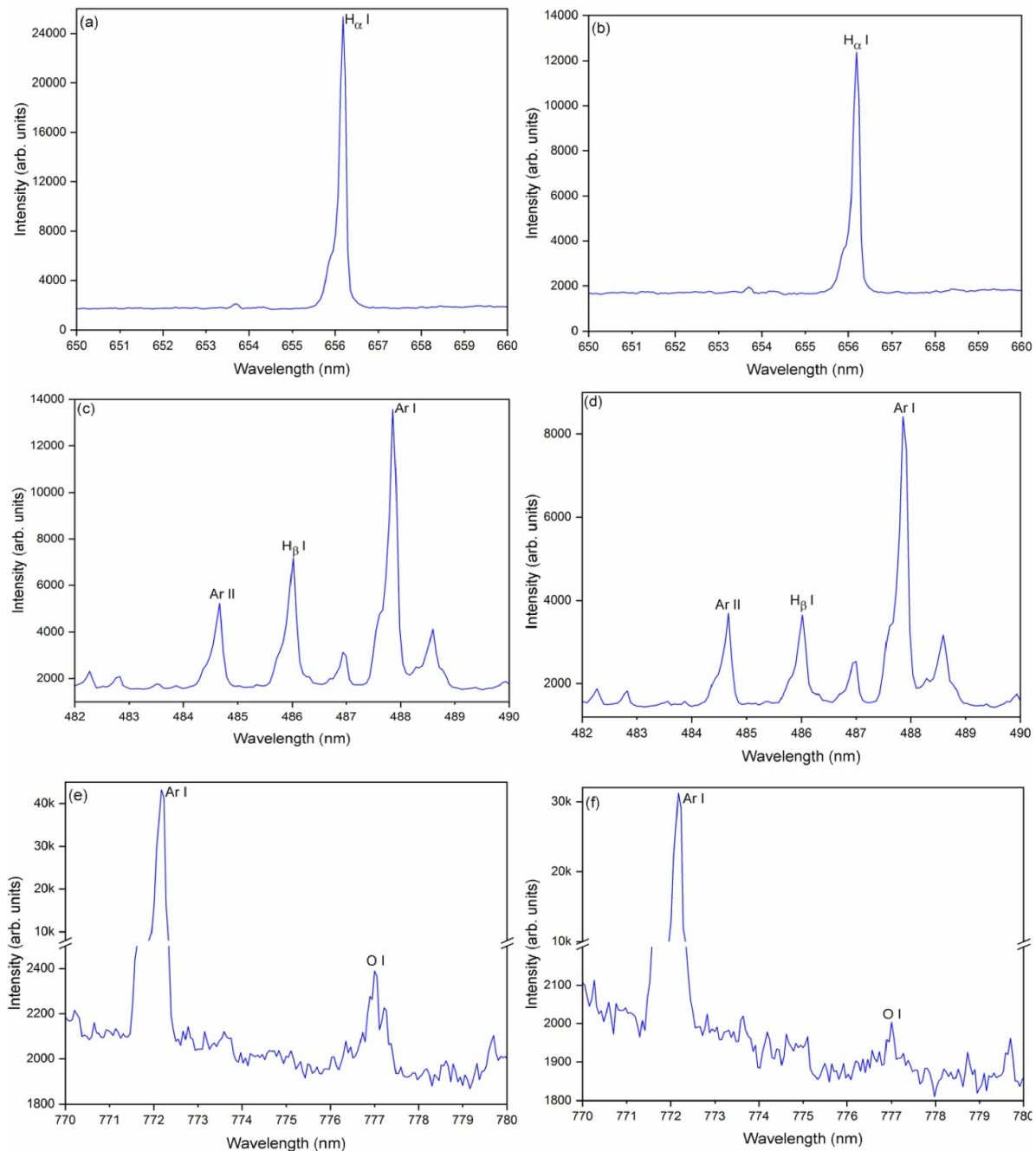


**Figure 5.** Intensity of various gas species observed during the etching procedure (a)  $H_{\alpha}$  I at the start of etching; (b)  $H_{\alpha}$  I at the end of etching; (c)  $H_{\beta}$  I, Ar I and Ar II at the start of etching; (d)  $H_{\beta}$  I, Ar I and Ar II at the end of etching; (e) Ar I and O I at the start of etching; (f) Ar I and O I at the end of etching. Substrates were in three-fold rotation and light collected from the overall chamber volume through a viewport.

a species with a constant density such as Ar. Comparison of figures 5(c) and (d) clearly demonstrates that  $H_{\beta}$  I intensity reduces with respect to Ar I.

The absolute intensities of these emission lines can be related to the density of the corresponding species inside the chamber during etching. Hence, it is very clear from this analysis that the density of atomic H and atomic O has decreased as etching has progressed. During the course of the substrate plasma pre-treatment process, the high substrate bias voltage

induces high energy ion bombardment of the substrate and sputters the surface releasing material into the chamber. The high-energy ion bombardment also releases secondary electrons, which are accelerated across the substrate sheath and contribute their energy to the bulk plasma in the vicinity of the substrate. This amplifies the excitation processes and generates an optically emitting auxiliary plasma near the surface of the substrates and explains the observed emission from H I, O I and Fe I. The O I emission was not detectable

without a substrate bias when there is no sputtering of the substrate surface and no auxiliary plasma. This confirmed that the emission corresponded to oxygen contamination being sputtered away from the substrate surface. Another possible source of oxygen atomic emission could be the dissociation of water vapour which has been chemisorbed from the substrate due to ion bombardment. This pathway would require several electron collisions to dissociate the water vapour, dissociate the hydroxyl group and excite the Oxygen atom. This sequence is less likely to occur in the relatively low-density plasma near the substrate compared to the sputtering of oxygen and its excitation.

The detection of Fe I emission confirmed that the substrate is being effectively decontaminated. The sputtering rate of Fe increases significantly once the contaminant compound ( $Fe_xO_y$ ) has been removed due to the factor 3.7 increase in sputter yields of Fe compared to  $Fe_2O_3$  [33]. Therefore the presence of Fe I indicates a clean surface.

The influence of electron temperature can be neglected due to the regulation of the etching parameters which ensures constant conditions including pressure, discharge current/plasma density, and bias voltage. Additionally, the contaminants which are eluted from the substrate comprise a relatively small fraction of the plasma density and therefore have a minimal effect on electron temperature.

A recommended strategy for identifying the end of substrate etching would utilise OE lines from atomic hydrogen and oxygen as these lines are intense (have high oscillator strengths) and the substrate as its emission intensified following the removal of oxide contamination. All of these emission lines have been detected during the etching process. The procedure would involve monitoring the relative intensities of the  $H_{\alpha}$  I and O I and substrate lines with respect to Ar I. A  $H_{\alpha}$  I and O I ratio drop of about 50% and detection of substrate lines could signify that the surface is sufficiently clean and that the etching step can be stopped. This corresponds to conditions achieved by substrate cleaning recipes established over a great number of process runs. This assumes that the Ar flow will be maintained constant throughout the etching step.

### 3.3. Control of coating thickness

Collecting light from the cathode surface at a grazing incidence using a ‘collimated’ detector located in the vacuum chamber above one of the sources allowed the intensity of metal emission to be measured and integrated over the duration of the process.

A series of depositions were carried out in a combined HIPIMS/DCMS deposition process of CrAlYN/CrN nanoscale multilayer. The conditions of sputtering were the same, while the duration of sputtering was varied. A linear correlation was found between the time-integrated intensity of the Cr I resonant line at 427.48 nm and the coating thickness (figure 6) with a correlation coefficient as high as 0.999.

The emission from Cr I is related to the density of Cr atoms, the density of exciting electrons, and the excitation rate coefficient which depends on the electron temperature. The intensity

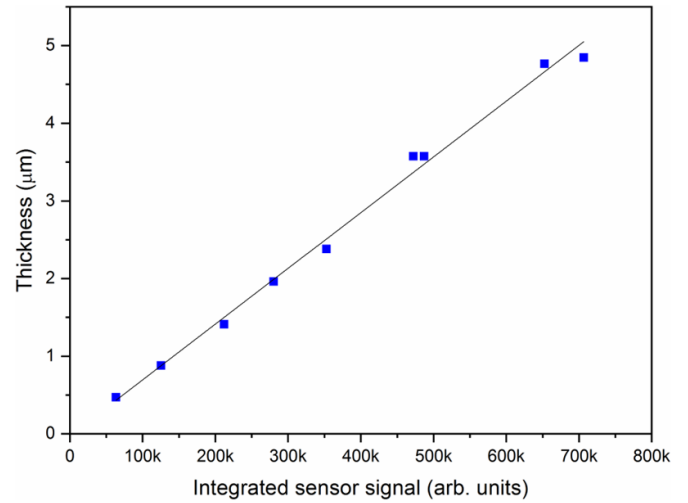


**Figure 6.** Thickness of the CrAlYN/CrN nanoscale multilayer coatings as a function of integrated signal intensity.

of emission is proportional to  $n_{Cr}n_e$ , where  $n_e$  is the electron density. Due to the quasineutral nature of plasmas, the electron density is similar to the ion density; on the other hand according to the definition of sputter yield, the ion density can be obtained by dividing  $n_{Cr}$  by the sputter yield. Combining these statements indicates that emission intensity is proportional to  $n_{Cr}^2$ . Reports have suggested that the discharge current is related linearly to the deposition rate and to the square root of the intensity of metal neutrals [34]. Our experimental data suggests that the thickness (which corresponds to the integral of metal flux over the process duration) and the integral of emission intensity over the process duration are linearly related. Considering that the flux and intensity may fluctuate during the process according to a Gaussian distribution, the coefficient of proportionality defined as the ratio of the two integrals can be given as:

$$s^{-1} = \frac{\int I_{CrI} dt}{\int n_{Cr}(t) v dt} = \frac{K_{Cr}^{exc} \int n_{Cr}^2(t) dt}{Y_{SV} \int n_{Cr}(t) dt} \sim \frac{1}{\sqrt{2}} \frac{\text{erf}\left(\frac{\langle n_{Cr} \rangle - n_{Cr}}{\Delta n_{Cr}}\right)}{\text{erf}\left(\frac{\langle n_{Cr} \rangle - n_{Cr}}{\sqrt{2} \Delta n_{Cr}}\right)} \quad (1)$$

where  $s$  is the coefficient of proportionality,  $K_{Cr}^{exc}$  is the excitation rate of Cr I emission,  $Y_S$  is the sputter yield of Cr by Ar,  $v$  is the arrival velocity of Cr atoms at the surface,  $n_{Cr}$  is the density of Cr in the vapour phase at a given time,  $\langle n_{Cr} \rangle$  is the average density and  $\Delta n_{Cr}$  is the average size of departure from the average density (standard deviation).

For stable processes the arrival flux is constant and  $n_{Cr} \approx \langle n_{Cr} \rangle$  the term on the right hand side of equation (1) evaluates to 1, so the ratio  $s$  is constant with time representing a linear relationship. For large fluctuations in the deposition flux of the order of  $10 \Delta n_{Cr}$ , the ratio tends to  $s/\sqrt{2}$ —a reduction of only 30%. This indicates that a linear relationship holds to within 30% even for strongly fluctuating deposition fluxes. This fits well with the experimental observations presented here and explains the linear relation between coating thickness and the integral of the emission intensity.

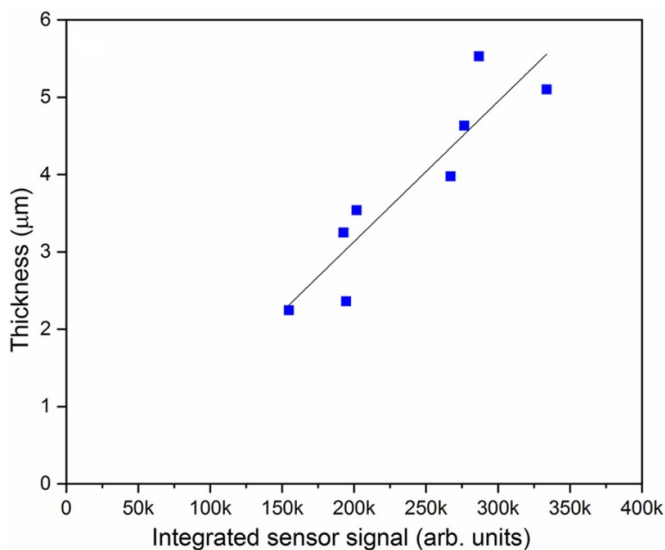


**Figure 7.** Thickness of V-based coatings as a function of integrated signal intensity—previous work.

To confirm this correlation, a similar analysis was carried out for a mixed sputtering and PACVD deposition process of a TiAlCN/VCN coating carried out in a Ar/N<sub>2</sub>/CH<sub>4</sub> atmosphere. The integral of V I intensity and coating thickness yielded a linear fit with a correlation coefficient of 0.91 (figure 7). In this example, the duration of deposition was fixed and the significant differences in deposition rate observed were due to operation at different partial pressure of reactive gas, which corresponded to a different poisoning degree of the target. In these conditions, the deposition was both from sputtering of the metal and deposition of carbon through a PACVD route, therefore monitoring the metal line and the carbon dissociation process, for example through the CN emission line, would have given a better approximation.

Although not demonstrated as part of the study, there seems little reason why a linear relationship should not apply to three, four and more component materials provided composition remains constant throughout. In the case of PACVD processes, such as the coating deposited at the industrial facility during the study, where Carbon becomes the dominant coating constituent, the linear relationship with the metal emission lines breaks down. Although work is still on-going to establish a relationship between OEs and coating thickness for this particular material, the use of film density as a factor in this relationship and employment of carbon-based molecule emission lines look promising.

### 3.4. Control of coating composition

It has been widely demonstrated that the composition of binary coatings, such as CrN, may be controlled, in reactive deposition, by adjusting the reactive gas flow to produce a pre-determined change in the intensity of a specific emission line from the metallic species compared to its value in the absence of reactive gas. This change in intensity is the result of target poisoning [30] and, in order to maintain the degree

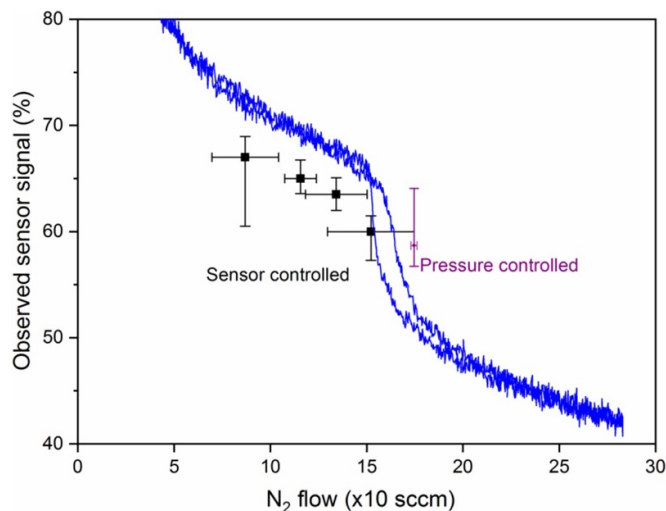


**Figure 8.** Hysteresis in observed sensor signal for Cr I (excited neutral atom) emission intensity at 425.435 nm as a function of nitrogen flow (blue line) and setpoints (squares) where films were deposited. ‘Error’ bars indicate the spread of values assumed by the sensor signal and gas flow over the entire duration of the process.

of poisoning required, it is common practice to control the reactive gas flow by means of a fast acting piezo-electric valve controlled by the OE signal intensity. However, before such an approach can be adopted it is necessary to experimentally establish the value of the fractional change in signal intensity required to maintain a particular composition. In the present case this was done for a CrAlYN/CrN coating by constructing a hysteresis curve for the OE sensor signal for Cr I (excited neutral atom) versus reactive (N<sub>2</sub>) gas flow for the CrAlY target [30], as shown in figure 8. Optical signals were obtained by monitoring the plasma immediately in front of magnetron using a ‘collimated’ detector located in the vacuum chamber above the sources.

During the deposition of a stoichiometric CrAlYN/CrN coating by the combined HIPIMS/UBM technique, the observed average sensor signal was found to be 58.7% as per the hysteresis curve displayed in figure 8. The hysteresis curve in figure 8 shows that higher sensor signals correspond to sputtering in metallic mode. Table 1 lists the nitrogen content in coatings deposited at various sensor set-points.

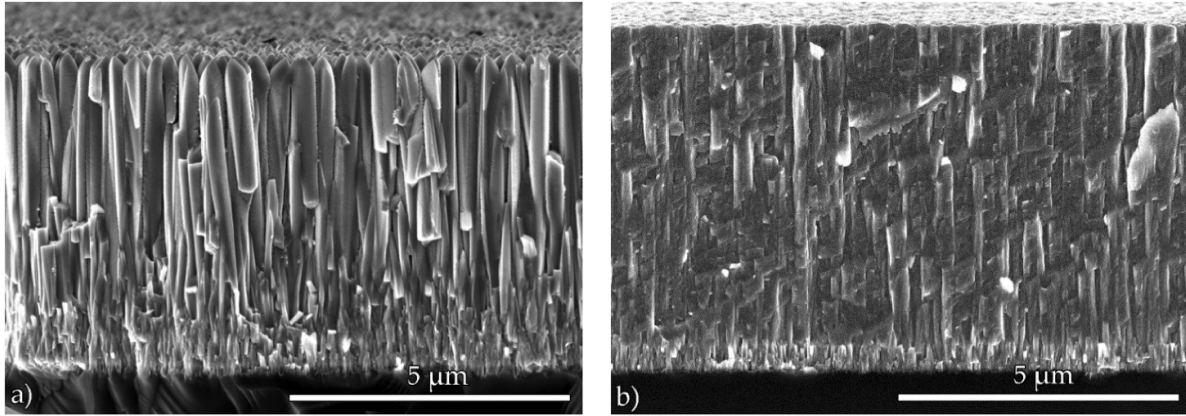
Figure 8 shows that operating in pressure control mode, resulted in a strong deviation in the sensor signal, which corresponds to variations in composition throughout the growth of the coating. Switching to OE control reduced the spread in sensor signal by a factor of 2 resulting in a more consistent coating composition.

The formation of (CrAl)<sub>2</sub>N phase was confirmed by XRD diffraction patterns (not shown), a change in morphology (figure 9), a change in deposition rate and nanohardness measurements (table 1).

XRD analyses of the coating with 43 at.% N deposited at setpoint 60 (not shown) revealed a clean fcc CrN pattern with a (111) crystallographic orientation, faceted crystal morphology, open intercolumnar boundaries (figure 9(a)) and low hardness (table 1). At nitrogen content of 40 at.% and below

**Table 1.** Properties of CrAlYN/CrN coatings deposited at different sensor set-points: Nitrogen content from SEM-EDX analysis, nanohardness and deposition rate.

Sensor setpoint (%)	Nitrogen content (at. %)	Nano-hardness (GPa)	Film thickness ( $\mu\text{m}$ )	Deposition rate ( $\mu\text{m h}^{-1}$ )	Phase composition (XRD)	Morphology (SEM)
60	43.7	9.7	5.6	1.6	CrN	Large crystals
63.5	40.0	17.8	5.7	1.7	CrAlN + (CrAl) <sub>2</sub> N	Nanocrystalline
65	30.2	17.5	6.2	1.9	(CrAl) <sub>2</sub> N + CrAl	Nanocrystalline
67	22.5	14	7.4	2.2	(CrAl) <sub>2</sub> N + CrAl	Nanocrystalline

**Figure 9.** Cross sectional SEM view of films of N content (a) 43.7 at.% CrAlN and (b) 30.2 at.% (CrAl)<sub>2</sub>N phase.

(setpoint  $\geq 63$ ), the XRD pattern switched to Cr<sub>2</sub>N. This was accompanied by a reduction in grain size and a film morphology comprising nano-grains, smooth surface and dense intercolumnar boundaries (figure 9(b)), which accounted for a high hardness of 17 GPa (table 1). These experiments have demonstrated improved control within the coating thickness itself. They also demonstrate the ability to synthesize both pure phases as well as a wide range of phase mixtures.

The reliable correlations between the emission intensity of film composition demonstrated here for a relatively complicated ternary nitride system established emission intensity as a reliable input which was used to inform the digital twin and make predictions on the composition of the film.

### 3.5. Coating texture, density and grain size

In addition to coating thickness and composition, coating texture, grain boundary density and grain size all have a marked impact on coating performance hence, to ensure reproducibility, it is important to be able to monitor, select and control these coating parameters. High fluxes of atomic nitrogen (low  $j_{Me/N}^S$ ) promote the formation of CrN dimers and trap metal on (200) and (220) surfaces which are metal rich compared to (111), thus promoting those textures. The surface energies are related as  $\gamma_{111} < \gamma_{110} < \gamma_{100}$  and due to the large gap between  $\gamma_{110}$  and  $\gamma_{100}$  typical of CrN [14], (220) surfaces emerge preferentially at intermediate energies before (200). Although atomistic studies of the CrAlN-based coatings under consideration here are not available, it can be assumed that similar processes are valid for those systems because Al atoms

are embedded as substitutes to Cr in a CrN fcc lattice up to a ratio of Al-to-total cations of 0.75 [35].

The ion-to-neutral ratio ( $j_{i/n}^S$ ) near the substrate is known [15, 16] to play an important role in determining adatom mobility which overcomes shadowing and promotes diffusion of adatoms into the grain boundaries resulting in densification of the film.

In this work we develop two optically-derived ratios ( $\mathcal{J}_{Me/N}^S$  and  $\mathcal{J}_{i/n}^S$ ) that are representative of the metal-to-dissociated nitrogen ratio ( $j_{Me/N}^S$ ) and the ion-to-neutral ratio ( $j_{i/n}^S$ ) in the deposition flux and overcome the challenges associated with obtaining precise quantitative. We also introduce an electrically-derived equivalent ( $\mathcal{D}$ ) to the plasma diffusion rate based on the ratio of current densities at the target and the substrate. The fundamental plasma quantities and their equivalents derived from easily accessible OE diagnostics and external process parameters are summarised in table 2 and discussed in detail in the following.

The ratios  $j_{i/n}^S$  and  $j_{Me/N}^S$  can be derived from the intensity of emission lines near the substrate, where these ratios correlate to film growth, however emission intensity is too low for reliable detection. On the other hand, the dense plasma region near the target surface provides strong emission intensity allowing for reliable measurement of  $j_{i/n}^T$  and  $j_{Me/N}^T$ . Taking into account the different rates of diffusion of ions and neutrals out of the magnetic confinement zone *en route* to the substrate, the target ratios  $j_{i/n}^T$  and  $j_{Me/N}^T$  can be corrected to represent a valid description of the ratios near the substrate  $j_{i/n}^S$  and  $j_{Me/N}^S$ .

The ratio of metal (Cr) and atomic nitrogen fluxes  $j_{Me/N}^T$  can be correlated to the ratio of line emission from Cr atoms and

**Table 2.** Fundamental plasma quantities and representative equivalents derived from real-time accessible plasma diagnostics and external process parameters.

Description	Quantity	Equivalent quantities derived from plasma and process parameter	
		At the target	At the substrate
Metal-to-dissociated nitrogen ratio	$J_{Me/N}^S \sim \frac{n_{Cr^{1+}} + n_{Cr^0}}{n_N}$	$\mathcal{N}_{Me/N}^T$	$\mathcal{J}_{Me/N}^S = \mathcal{D} \mathcal{N}_{Me/N}^T$
Ion-to-neutral ratio	$J_{i/n}^S \sim \frac{n_{Cr^{1+}} + n_{N_2^{1+}} + n_{Ar^{1+}}}{n_{Cr^0}}$	$\mathcal{N}_{i/n}^T$	$\mathcal{J}_{i/n}^S = \mathcal{D} \mathcal{N}_{i/n}^T$
Plasma diffusion rate	$D$	$\mathcal{D} = \frac{I_{bias} A_S^{-1}}{I_d A_T^{-1}}$	

N<sub>2</sub> molecules. Cr atoms are produced by the sputtering process where Ar ions bombard the target and knock out surface atoms. Cr atom density,  $n_{Cr^0}$ , is proportional to the sputter yield,  $Y_S$ , and plasma density,  $n_e$  [36].

$$n_{Cr^0} = Y_S n_e 0.6e \sqrt{\frac{kT_e}{m_{ion}}} (1 - \gamma) = n_e K_S \quad (2)$$

$$n_e = n_{Cr^0} / K_S \quad (3)$$

where  $e$  is the electron charge,  $k$  is the Boltzmann constant,  $T_e$  is the electron temperature,  $m_{ion}$  is the mass of sputtering ion,  $\gamma$  is the secondary electron emission coefficient and  $K_S$  is the sputter rate coefficient.

The emission from Cr atoms is excited via electron collisions and its intensity is related to the electron density, Cr atom density  $n_{Cr^0}$ , and temperature-dependent excitation coefficient of Cr ( $K_{Cr}^{exc}$ ), the latter term allowing for the effect of electron temperature [34, 37]. Thus, the intensity of emission from Cr atoms ( $I_{CrI}$ ) is related to  $n_{Cr^0}^2$  and the electron temperature-dependant excitation rate coefficient ( $K_{Cr}^{exc}$ ). The density of Cr atoms is related to the intensity as:

$$n_{Cr^0} = \left( I_{CrI} \frac{K_S}{K_{Cr}^{exc}} \right)^{0.5} \quad (4)$$

Chromium ions, Cr<sup>1+</sup>, are produced by electron ionisation collisions with Cr atoms. The density of Cr<sup>1+</sup>,  $n_{Cr^{1+}}$ , is related to  $n_{Cr^0}$ , the electron density, the ionisation rate coefficient for Cr<sup>0</sup>,  $K_{Cr}^i$  and the recombination rate coefficient for Cr<sup>1+</sup>,  $K_{Cr}^r$  [38]. Combining with equations (2)–(4) the density of Cr<sup>1+</sup> ions can be expressed in terms of the Cr neutral intensity,  $I_{CrI}$ , as

$$n_{Cr^{1+}} = I_{CrI} \frac{K_{Cr}^i}{K_{Cr}^r} \frac{1}{K_{Cr}^{exc}} \frac{1}{n_e} \quad (5)$$

Atomic nitrogen is predominantly produced by electron collisions that dissociate N<sub>2</sub> molecules in the working gas. Atomic nitrogen then diffuses towards the substrate undergoing elastic scattering reactions. A second major mechanism is by dissociation of molecular Nitrogen ions colliding with the substrate surface with high energy. The bias voltage of –65 V is sufficient to cause a significant proportion of N<sub>2</sub><sup>+</sup> to be dissociated in this way. In both pathways the emission intensity of N<sub>2</sub> is a good indicator of the amount of

atomic nitrogen in the system as the differences between excitation, ionisation and dissociation energies of N<sub>2</sub> are small [39]. Molecular Nitrogen emission is excited in a similar way as molecular dissociation, predominantly through electron collisions and its intensity depends on the density of electrons, their temperature and the excitation coefficient,  $K_{N_2}^{exc}$ . Molecular Nitrogen emission ( $I_{N_2}$ ) is proportional to the density of dissociated nitrogen atoms  $n_N$  to the substrate through the ratio between the rate coefficients for dissociation  $K_{N_2}^d$  and excitation  $K_{N_2}^{exc}$ , where the ratio is a known function of the electron temperature.

$$n_N = I_{N_2} \frac{K_{N_2}^d}{K_{N_2}^r} \frac{1}{K_{N_2}^{exc}} \frac{1}{n_e} \quad (6)$$

where  $K_{N_2}^r$  is the recombination rate coefficient.

Assuming equilibrium conditions, the velocity of ions would be constant and the flux proportional to the density.

For the second mechanism, the flux of molecular N<sub>2</sub><sup>+</sup> ions will convert to dissociated nitrogen flux for impingement energies beyond 20 eV. Analogous to  $n_N$ , the density of N<sub>2</sub><sup>+</sup> molecular ions is

$$n_{N_2^+} = I_{N_2} \frac{K_{N_2}^i}{K_{N_2}^r} \frac{1}{K_{N_2}^{exc}} \frac{1}{n_e} \quad (7)$$

where  $K_{N_2}^i$  is the rate coefficient for ionisation of N<sub>2</sub>,  $K_{N_2}^r$  for recombination and  $K_{N_2}^{exc}$  for excitation.

The ion-to-neutral flux ratio at the target can be obtained by combining equations (2) through (7):

$$\begin{aligned} j_{i/n}^T &\sim \frac{n_{Cr^{1+}} + n_{N_2^+} + n_{Ar^+}}{n_{Cr^0}} \\ &\sim n_e^{-1} \left( I_{CrI} \frac{K_{Cr}^i}{K_{Cr}^r} \frac{1}{K_{Cr}^{exc}} + I_{N_2} \frac{K_{N_2}^i}{K_{N_2}^r} \frac{1}{K_{N_2}^{exc}} + I_{ArI} \frac{K_{Ar}^i}{K_{Ar}^r} \frac{1}{K_{Ar}^{exc}} \right) \\ &\quad \times \left( I_{CrI} \frac{K_S}{K_{Cr}^{exc}} \right)^{-0.5} \end{aligned} \quad (8)$$

where  $K_{Ar}^i$  is the rate coefficient for ionisation of Ar and  $K_{Ar}^r$  for recombination. A general representation of  $j_{i/n}^T$  would include multiple-charged metal ions in the numerator. However we estimate these to be negligible as at typical deposition pressures of  $3 \times 10^{-3}$  mbar and deposition distances of 100 mm the majority of these would undergo charge exchange with

Ar atoms and would not reach the substrates, as previously discussed in detail [40].

The metal-to-nitrogen flux ratio at the target can be obtained by combining equations (4)–(7) and simplifying:

$$j_{Me/N}^T \sim \frac{n_{Cr^{1+}} + n_{Cr^0}}{n_N + n_{N_2^+}} \sim \left( I_{CrI} \frac{K_S}{K_{Cr}^{exc}} \right)^{0.5} \left[ I_{N_2} \frac{1}{K_{N_2}^{exc}} \frac{1}{n_e} \left( \frac{K_{N_2}^d}{K_{N_2}^{rd}} + \frac{K_{N_2}^i}{K_{N_2}^{ri}} \right) \right]^{-1} \quad (9)$$

where we have assumed that  $\left( \frac{K_S}{K_{Cr}^{exc}} \right)^{0.5} \gg \frac{K_{Cr}^i}{K_{Cr}^{exc}} \frac{1}{n_e}$ .

The ratios in ionisation and excitation rate coefficients in equations (8) and (9) are affected by the electron temperature. The variation in electron temperature was estimated from the ratio of emission line intensities from  $N_2^{1+}$  and  $N_2$  and correcting for changes in plasma density as derived from the peak discharge current density:

$$T_e \sim \mathcal{T}_e \equiv \frac{I_{N_2^{1+}}}{I_{N_2}} J_d^{-1} \quad (10)$$

Within the parameter space explored, the ratio of emission line intensities from  $N_2^{1+}$  and  $N_2$  declined from 0.4 to 0.2 and plasma density increased by 25% as derived from the peak discharge current density increase from 0.3 to 0.38 A cm<sup>-2</sup>. The ratios in ionisation and excitation rate coefficients in equations (8) and (9) were considered to vary linearly with the electron temperature and, since not all of the coefficients are available in the literature, are considered equal to each other as a first approximation. The ratios of ionisation and recombination coefficients were considered constant with temperature [41].

We define optically-derived ratios, which are related to physical ratios through a constant of proportionality as follows:

$$\mathcal{N}_{i/n}^T \equiv n_e^{-1} \left( I_{CrI} \frac{K_{Cr}^i}{K_{Cr}^{exc}} \frac{1}{K_{Cr}^{exc}} + I_{N_2} \frac{K_{N_2}^i}{K_{N_2}^{exc}} \frac{1}{K_{N_2}^{exc}} + I_{ArI} \frac{K_{Ar}^i}{K_{Ar}^{exc}} \frac{1}{K_{Ar}^{exc}} \right) \times \left( I_{CrI} \frac{K_S}{K_{Cr}^{exc}} \right)^{-0.5} \mathcal{T}_e \quad (11)$$

and

$$\mathcal{N}_{Me/N}^T \equiv \left( I_{CrI} \frac{K_S}{K_{Cr}^{exc}} \right)^{0.5} \left[ I_{N_2} \frac{1}{K_{N_2}^{exc}} \frac{1}{n_e} \left( \frac{K_{N_2}^d}{K_{N_2}^{rd}} + \frac{K_{N_2}^i}{K_{N_2}^{ri}} \right) \right]^{-1} \mathcal{T}_e \quad (12)$$

In the results described in the following section,  $\mathcal{N}_{i/n}^T$  and  $\mathcal{N}_{Me/N}^T$  were calculated using lines of low and high excitation (upper) levels and exhibited similar trends versus the coil current confirming the approach.

The dissociation degree of nitrogen in the plasma was estimated using actinometry [42, 43]. The method relies on the measurement of the relative intensity of dissociated nitrogen and argon obtained from  $N(2p^4P^o) \rightarrow N(3s^4P)$

(818–825 nm, 7-plet) and  $Ar(2p_9) \rightarrow Ar(1s_5)$  (811.5 nm) transitions. The degree of dissociation of nitrogen is given by

$$\frac{n_{N^{(4S)}}}{n_{N_2}} \sim U_d \frac{I_N}{I_{Ar}} \quad (13)$$

where  $n_{N^{(4S)}}$  is the density of atomic nitrogen,  $n_{N_2}$  is the density of molecular nitrogen,  $U_d$  is the discharge voltage,  $I_N$  is the emission intensity from atomic nitrogen ( $N I$ ) and  $I_{Ar}$  is the emission intensity of argon neutrals ( $Ar I$ ). The above expression holds under the assumption of a constant Ar:N<sub>2</sub> content in the chamber and a linear relationship between the ratio of excitation coefficients of  $Ar (K_{Ar}^{exc})$  and  $N (K_N^{exc})$  and the discharge voltage  $\frac{K_{Ar}^{exc}}{K_N^{exc}} \sim E \sim U_d$ , where  $E$  is the electric field in the bulk plasma.

In the following section we explore the variation in optically-derived ratios as a function of unbalancing coil current and their relation to the microstructure and texture of the deposited coatings. The unbalancing coil current changed the width of the racetrack and the height of the confinement tunnel. Magnetic field simulations were used to calculate the cross sectional area of the tunnel and the volume of plasma trapped within the racetrack.

The optically-derived ion-to-neutral ratio near the target  $\mathcal{N}_{i/n}^T$  was found to reduce monotonically with coil current reaching a two-fold decrease (figure 10(a)). The reduction could be attributed to a seven-fold constriction in the racetrack volume where the majority of ionisation collisions occur. This is balanced by a 1.75-fold narrowing of the racetrack area of the target, where the majority of sputtered neutral species are created.

The optically-derived ratio of metal vapour to dissociated nitrogen near the target  $\mathcal{N}_{Me/N}^T$  was found to increase by a factor of 2.0 reaching a maximum at a coil current of 4 A (figure 10(b)) and gradually reducing as the coil current rose beyond that. Meanwhile the atomic nitrogen dissociation rate  $n_{N^{(4S)}} : n_{N_2}$  (figure 10(c)) went through a minimum at a coil current of 4 A. The above mentioned narrowing and constriction of the racetrack increases power density by a factor 1.4 which is outweighed by the seven-fold reduction in volume for ionisation and dissociation. These factors combine to increase the metal-to-dissociated nitrogen ratio up to a coil current of 4 A. Beyond 4 A, the dissociation of nitrogen increases whilst metal sputtering rates continue to drop leading to a reduction in  $\mathcal{N}_{Me/N}^T$ .

To describe the film growth environment, it is crucial to determine the plasma chemistry near the substrate which is governed by the diffusion of plasma species from the target to the substrates. The ratios  $\mathcal{N}_{i/n}^T$  and  $\mathcal{N}_{Me/N}^T$  discussed thus far are derived from optical observations of the dense plasma region of the magnetron cathode and correspond to the plasma composition near the target. Target plasma diffuses towards the substrate at a rate,  $D$ , which in this system is primarily dependent on the degree of unbalancing of the confining magnetic field at the cathode, and is controlled by the current-driven unbalancing coils that strengthen the outer magnetic poles of the cathodes. This regulates the proportion

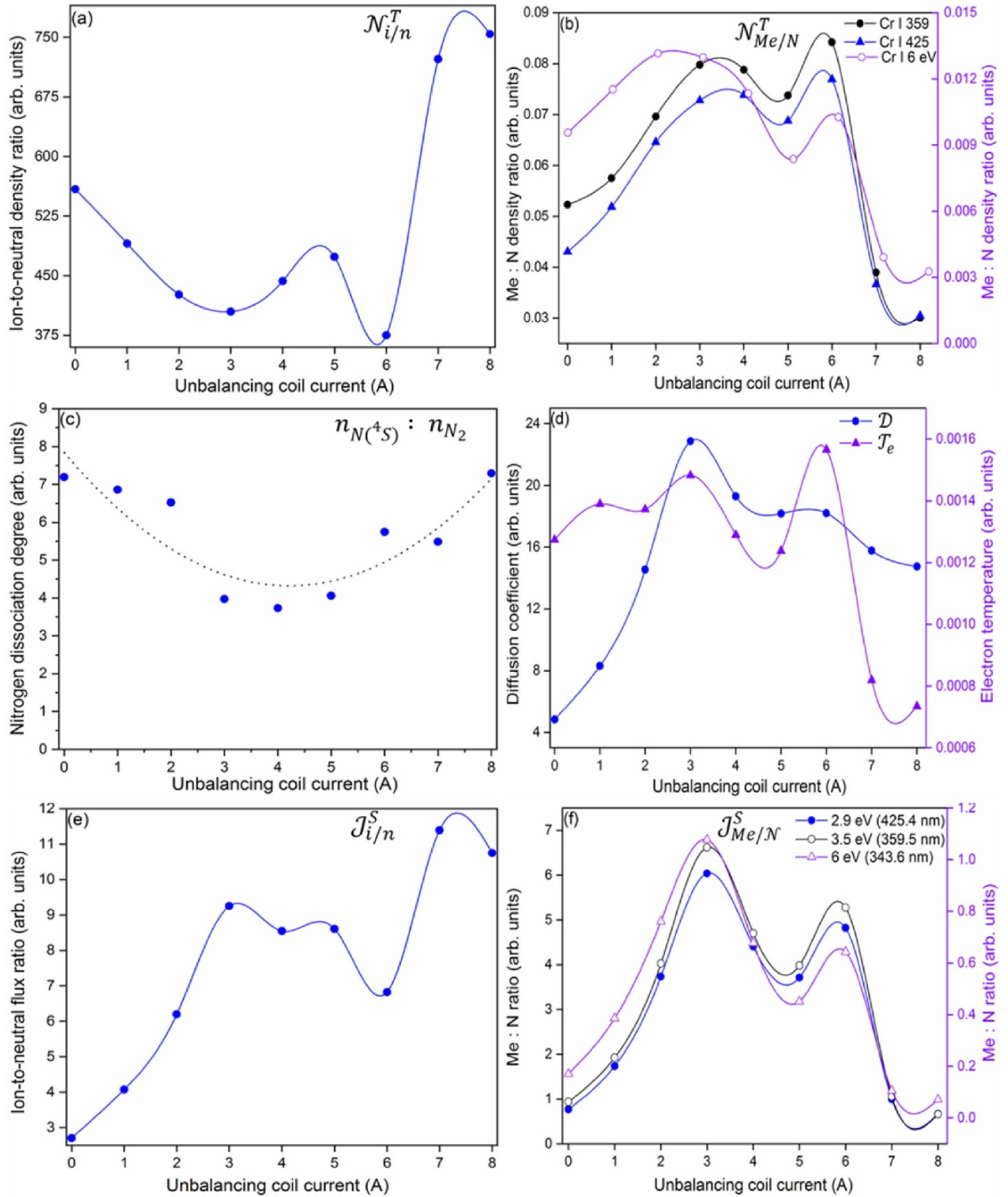


**Figure 10.** Influence of coil current on the properties of the deposition flux: (a)  $\mathcal{N}_{i/n}^T$  optically-derived ion-to-neutral density ratio at the target; (b)  $\mathcal{N}_{Me/N}^T$  optically-derived Me:N density ratio at the target; (c)  $n_{N(4S)} : n_{N_2}$  nitrogen dissociation degree; (d)  $\mathcal{D}$  plasma diffusion rate derived from target and substrate current densities; (e)  $\mathcal{J}_{i/n}^S \times 10$  optically-derived ion-to-neutral flux ratio at the substrate; (f)  $\mathcal{J}_{Me/N}^S \times 10^{-3}$  optically-derived Me:N flux ratio at the substrate estimated using Cr I emission lines with low and high excitation energies.

of discharge current reaching the substrates as represented by the ratio of substrate to discharge current densities,

$$\mathcal{D} = \frac{I_{bias} A_S^{-1}}{I_d A_T^{-1}} \sim \mathcal{D} \quad (14)$$

where  $I_{bias}$  is the substrate bias current,  $A_S$  is the substrate area,  $I_d$  is the discharge current and  $A_T$  is the racetrack area. Since  $A_S$  is constant in this experiment,

$$\mathcal{D} = \frac{I_{bias} A_S^{-1}}{I_d A_T^{-1}} \sim \frac{I_{bias}}{I_d A_T^{-1}} \quad (15)$$

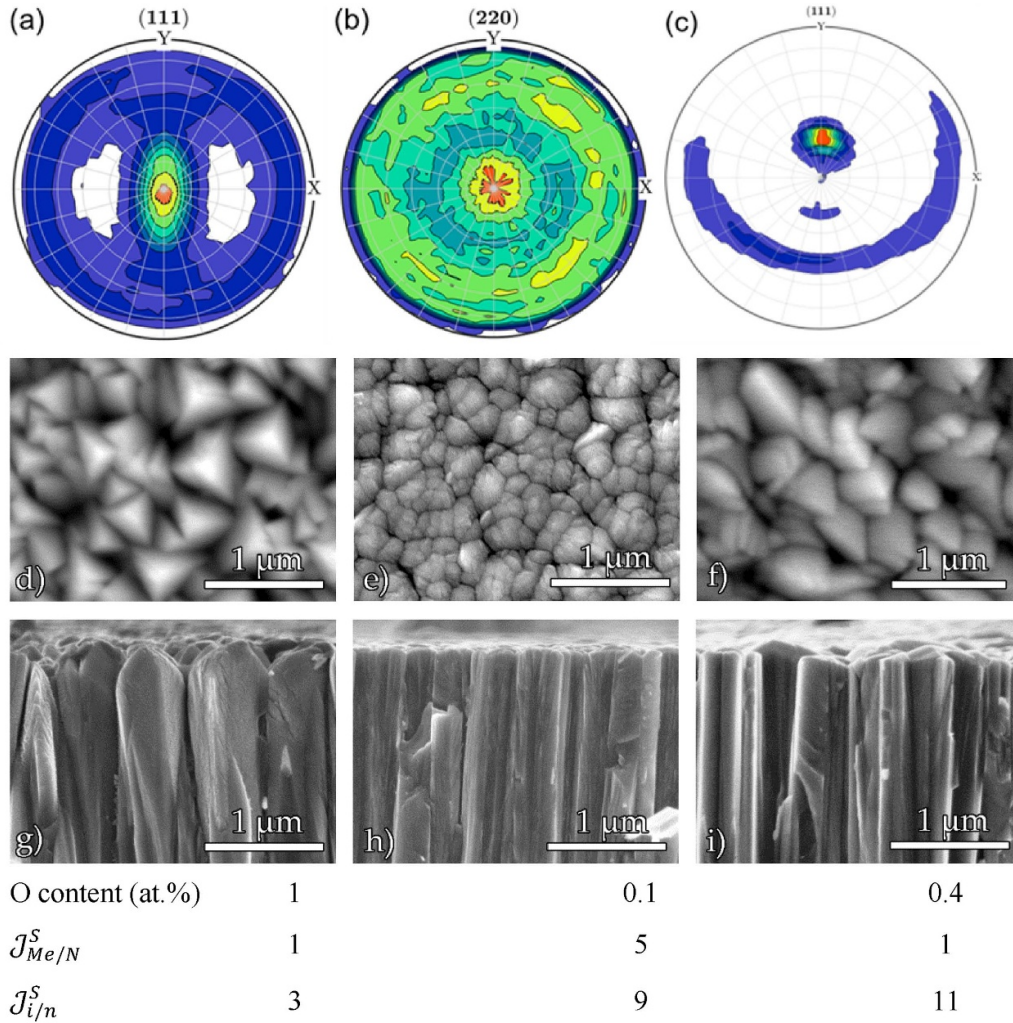


**Figure 11.** Pole figures illustrating the preferred out of plane crystallographic texture of a CrAlN-based coating for (a)  $I_{coil} = 0$  A—(111) surface, (b)  $I_{coil} = 4$  A—(220) surface and (c)  $I_{coil} = 7$  A—inclined (111) surface. SEM images showing the surface morphology of the films deposited at (d)  $I_{coil} = 0$  A, (e)  $I_{coil} = 4$  A and (f)  $I_{coil} = 7$  A. Cross-sectional SEM views of the films deposited at (g)  $I_{coil} = 0$  A, (h)  $I_{coil} = 4$  A and (i)  $I_{coil} = 7$  A.

Figure 10(d) shows that  $\mathcal{D}$  varies significantly with coil current by as much as a factor of 4. As the magnetic field does not influence the neutral portion of the metal vapour flux to the substrate, the overall effect is that the diffusion rate describes not only the ion component of the substrate flux but also relates to the ion-to-neutral ratio.

The composition of the flux to the substrate is a combination of the plasma chemistry created at the target and diffusivity of the plasma towards the substrates and can be approximated by the product of plasma diffusivity  $\mathcal{D}$  and the optically-derived plasma chemistry ratios—the ion-to-neutral ratio  $\mathcal{N}_{i/n}^T$  and metal vapour to dissociated nitrogen ratio  $\mathcal{N}_{Me/N}^T$ . The optically-derived ion-to-neutral and metal-to-dissociated nitrogen ratios at the substrate are thus:

$$\mathcal{J}_{i/n}^S = \mathcal{D} \mathcal{N}_{i/n}^T \sim j_{i/n}^S \quad (16)$$

and

$$\mathcal{J}_{Me/N}^S = \mathcal{D} \mathcal{N}_{Me/N}^T \sim j_{Me/N}^S \quad (17)$$

The ratios were obtained by real-time OE monitoring of the intensity of  $N_2$  I (315.969 nm) ( $C^3\Pi_u - B^3\Pi_u$  second positive system), Cr I (425.4 nm), Cr I (343.619 nm) and Ar I (810.3693 nm) lines details of which are given in table A1 of the appendix. The electrically-derived plasma diffusivity  $\mathcal{D}$  was obtained from measurements of the peak substrate current,  $I_{bias}$ , and the width of the racetrack obtained from simulations of the magnetic field. Figures 10(e) and (f) show that both  $\mathcal{J}_{i/n}^S$  and  $\mathcal{J}_{Me/N}^S$  exhibit significant variations with coil current and undergo a maximum at 3 A.

$\mathcal{J}_{Me/N}^S$  and  $\mathcal{J}_{i/n}^S$  correlate strongly with the preferred crystallographic texture, grain morphology and grain size of the films.

The variation in  $\mathcal{J}_{Me/N}^S$  revealed a threshold of  $\sim 1.5$  where the crystallographic texture switched from (111) to (220) as shown in the pole figures in figures 11(a)–(c). Meanwhile,  $\mathcal{J}_{i/n}^S$  affected the density of intercolumnar boundaries with a minimum level of  $\sim 3$  required to achieve high density as shown in the cross-sectional SEM views in figures 11(g)–(i) and the drastically reduced oxygen content in the films. For

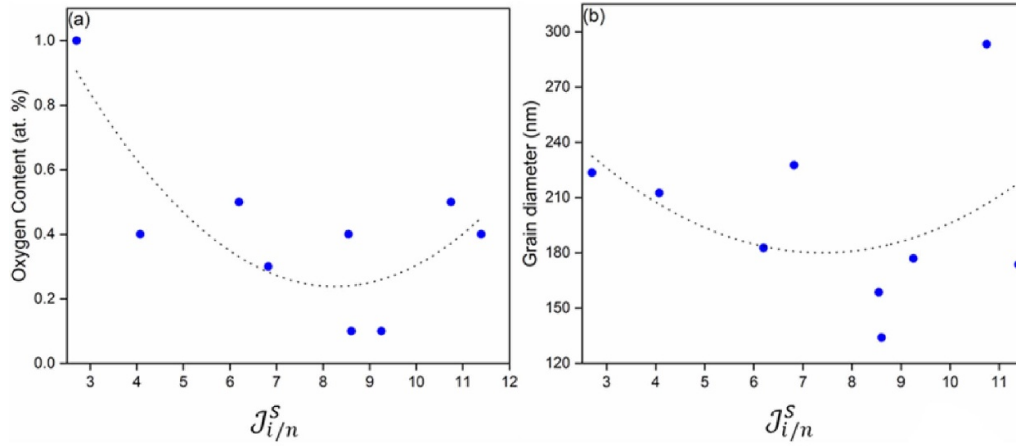


**Figure 12.** Oxygen content (a) and grain diameter (b) as a function of  $\mathcal{J}_{i/n}^S$ .

coil currents of 1–6 A,  $\mathcal{J}_{Me/N}^S$  remained above the threshold and the dominant crystal orientation in the films was (220).  $\mathcal{J}_{i/n}^S$  was above the threshold for coil currents greater than 1 A and the density of the films was high as evidenced both by the dense grain boundaries (figures 11(b)–(h)) and the low oxygen content. Unexpectedly, at high coil currents (7 and 8 A) the dominant orientation switched back to (111) (figure 11(c)) and the texture was tilted by  $\sim 22$  degrees off normal. The microstructural density was reduced compared to coil currents of 3 A due to a switch in preferred orientation from 220 to 111, however the density was improved relative to 0 A as seen in the cross sectional SEMs and oxygen content due to the high  $\mathcal{J}_{i/n}^S$  (see discussion below).

For  $\mathcal{J}_{Me/N}^S < 2$ , the grain morphology was faceted (figures 11(d) and (f)) and typical of a strong (111) crystallographic orientation in which grain surfaces expose a densely packed atomic structure which is impervious to contaminant phases and which pushes contaminant atoms towards the grain boundaries. Once there, the contaminants bind deposition atoms and arrest their diffusion into intercolumnar voids thus leaving them open. For  $\mathcal{J}_{Me/N}^S > 2$  the orientation switches to (220) which is an open crystal lattice configuration which is able to absorb and dissolve contaminants, leaving grain boundaries clean and free for deposition atoms to diffuse into and fill [15, 20].

As a result of the high  $\mathcal{J}_{i/n}^S > 3$ , intercolumnar voids were densified by the deposition material and the grain morphology was significantly smoother.

$\mathcal{J}_{i/n}^S$  is a good predictor for coating density. The deposition at very high coil currents presented an interesting case where  $\mathcal{J}_{Me/N}^S$  is low but  $\mathcal{J}_{i/n}^S$  is relatively high. As  $\mathcal{J}_{Me/N}^S$  drops below the threshold of 2, a (111) texture is promoted, similar to the 0 A deposition. However  $\mathcal{J}_{i/n}^S$  remains significantly higher than at 0 A, which increases adatom mobility into grain boundaries thus helping to densify the (111) microstructure.

The density of the films is linked to the oxygen content in the films, which is mostly absorbed in intercolumnar grain boundaries. Figure 12(a) illustrates a good correlation between  $\mathcal{J}_{i/n}^S$  and the oxygen content obtained by EDX. A

good correlation is also obtained between  $\mathcal{J}_{i/n}^S$  and the grain size as derived from plan-view SEM images (figure 12(b)). The clear correlations observed serve as additional evidence for the validity of the optically-derived parameters.

The nitrogen dissociation degree at the target (figure 10(c)) did not map well with the observed development of preferred texture, reaching its lowest value at a coil current of 3 A, where  $\mathcal{J}_{Me/N}^S$  and  $\mathcal{J}_{i/n}^S$  were at a maximum. Therefore in these experiments the nitrogen dissociation degree at the target alone was a poor indicator for texture because it fails to consider variations in metal vapour flux. In magnetron sources, the dissociation of the gas and production of metal vapour are both driven by the plasma density and power dissipated in the discharge, and can rarely be controlled independently. Any analysis requires a holistic approach including the effect on metal as well as dissociated gas.

The preferred crystallographic texture, morphology and density of a CrAlN-based coating were successfully controlled using optically-derived ion-to-neutral ratio  $\mathcal{J}_{i/n}^S$  and metal vapour to dissociated nitrogen ratio  $\mathcal{J}_{Me/N}^S$ . The strategy can be applied in a real-time/low latency scenario of monitoring a PVD process, calculating the ratios and predicting the resulting coating properties. It can serve as an efficient classifier indicating whether the growth conditions are diffusion limited or reaction rate limited and whether the crystallographic orientation is likely to be 111, 220 or 200 as well as predicting the porosity of the films.

The applicability of the strategy can be broadened to other coating materials, by establishing experimentally the threshold values of  $\mathcal{J}_{Me/N}^S$  and  $\mathcal{J}_{i/n}^S$  for preferred texture formation and grain boundary densification.

### 3.6. Chamber condition monitoring

The study considered how OES could be used to address the three principal roles of chamber condition monitoring, viz to identify in real-time: (1) conditions that would compromise the production potential of coating equipment; (2) conditions that would have a negative impact on coating integrity and/or coating equipment; and (3) sub-system malfunction.

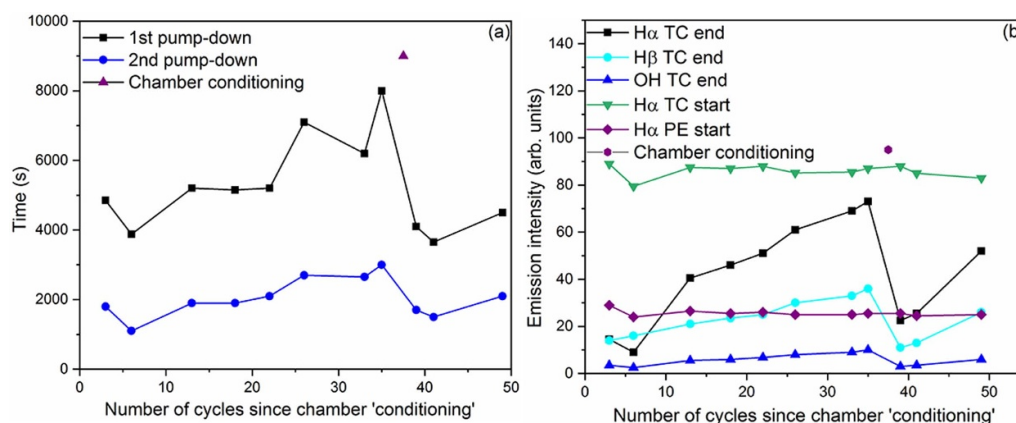


**Figure 13.** Chamber condition monitoring over 49 production cycles (a) pump-down times and target cleaning periods and (b) emission intensity of H $\alpha$ , H $\beta$  and OH lines at the start and finish of target clean and start of plasma etch phases.

The production potential of coating equipment could be compromised by out-gassing of air and water vapour absorbed during chamber loading/unloading; materials (water, cleaning fluids, oil or grease) trapped in cavities in components being coated; air or water leaks resulting from, e.g. damage to seals during between-cycle maintenance; or thermal breakdown of coating deposited onto chamber walls/heater elements during previous coating cycles. These manifest themselves by pump-down times exceeding a predefined limit, and OES can be used to identify the cause of such extended pump-down.

Coating and equipment integrity could be compromised by external (air) leaks and internal (water) leaks which could be prevented by identification and highlighting in real-time.

Sub-system malfunctions include failure, of a number of different equipment sub-systems, such as loss of power to coating sources (magnetron(s) or evaporation source(s)); failure or malfunction of one or more gas flow controllers; failure of heater elements, etc.

Figure 13(a) illustrates the variation in pump-down times over 48 production cycles. The initial cycles are operated in a clean chamber following a chamber conditioning procedure and achieve the minimum pump down times of 5200 s. Over 30 cycles, the time increases by 210% to 11 000 s due to gradual build-up of contamination layer on the grounded chamber walls consisting of Cr, C, N, H from process gases. Due to the electrical grounding, the deposition flux to the chamber walls is of low energy and the resulting contamination layer contains a large number of pores which readily pick up oxygen and water vapour during loading. During the process, contamination is released resulting in longer pump-down times and is incorporated into the coating. Figure 13(b) shows that the H $\alpha$  I emission intensity measured at the end of the target cleaning process step exhibits very large changes with cycle and appear to be more sensitive to chamber contamination than the pump down times in figure 13(a). A response is also seen for OH and H $\beta$  I emission although at a lower level. Interestingly the emission intensity of these species measured

at the start of target cleaning or plasma etching did not correspond well to chamber contamination.

In the majority of cases, process deviations will be readily detectable using real-time monitoring of both absolute and rate-of-change of various OES signals using an 'Optix' style optical gas analyser with internal plasma excitation, operating in the range 0.5–10<sup>-6</sup> mbar and comparing these with 'normal' values established using 'historical' data. If incorporated into process control software such real-time monitoring should automatically trigger alarm signals, which in critical cases should initiate safe shut-down of the equipment to avoid coating degradation or equipment damage.

In the absence of air and water leaks (see below), for compromised production potential the most relevant lines to monitor are H $\alpha$ , H $\beta$  and OH, at 656, 485 and 309.6 nm. The best way of identifying compromised production potential (e.g. extended pump-down associated with coating build-up) is to monitor the rate of fall of intensity of one of the lines at a specific intensity or to choose an intermediate time point and determine the intensity of one or all of the lines at that time point. A predefined limit on one or other (or both) of these measures, which would need to be established experimentally, can be used to identify when an 'interventionary' measure, such as a chamber clean/replacement of chamber shields, or a 'conditioning cycle', is required.

Alternative causes of compromised production potential are the release of gaseous fragments from the breakdown of thermally unstable coatings or low melting point materials deposited on or in the vicinity of heater elements during previous coating cycles, and emissions resulting from ineffective cleaning/drying of components for coating, all of which will contribute to the pumping load during chamber evacuation. OES offers a convenient means of identifying such gaseous fragments, although condensable volatile material might present more of a challenge, depending on the type of OES system in use. Identifying the presence and nature of contaminants being released into the vacuum space could make a major contribution to coating quality by supporting

the development and deployment of mitigation strategies, for example, between-cycle cleaning of heater elements or use of chromium (or other refractory metal) ‘conditioning’. In the absence of such mitigation, the release of such material might result in contaminant deposition on substrates leading to a degradation of the substrate-coating interface or contamination of the deposited layer.

For air and water leaks, early detection will have a major impact on reducing production delays, avoiding the need for costly reworking or, at worse, scrapping of product with compromised coatings resulting from contamination by air or water.

Air leaks are most likely to occur during between-cycle maintenance/cleaning operations and can best be detected during evacuation, target clean and substrate etching by monitoring the intensity and rate-of-change of the  $N_2$  (C–B) emission line at 336.7 nm, though the limiting values identifying the presence of leaks will need to be established experimentally. For coating deposition stages, monitoring the intensity of the same line might be sufficient, although in the case of deposition of a nitrogen containing layer, the absolute value of intensity of O I emission at 777.194 nm should be used. For films containing both N and O, monitoring of OH emission at 309.6 nm should be considered, although this will not allow differentiation between air and water leaks—see below for monitoring for water leaks. In all cases it will be necessary to experimentally establish the limiting values of line intensities and/or their rate-of-change to indicate the presence or otherwise of a leak.

Unlike air leaks, water leaks are unlikely to occur as a result of between-cycle maintenance and cleaning operations but are more likely to result from operations such as replacement of directly cooled targets, although another source is corrosion related pin-holes in water cooled, vacuum facing surfaces. Whilst very minor leaks might have a minimal effect on coating quality and integrity, any water leak in a vacuum system is undesirable as it will inevitably lead to increased evacuation times and might seriously impact coating adhesion, composition, microstructure, mechanical/aesthetic properties and functionality. OES provides a means of real-time detection of water leaks occurring at any point in a coating cycle, typically by monitoring the intensity and rate of fall of OH emission at 309.6 nm.

In the case of sub-system failure, although not forming part of the study, real-time monitoring with OES could also be used to identify, for example failure of magnetron (or evaporation source) power supply, substrate power supply, mass flow controllers, radiant heater elements and sample rotation.

These and other examples of sub-system malfunction will be readily detected through the occurrence of unanticipated changes to OES lines associated with the malfunctioning device(s), e.g. magnetrons (metallic species), substrate power supply and mass flow controllers (process gas species), heater elements (‘remnant’ species, in particular OH), or sample rotation (loss of periodic variations of metallic lines intensity).

Whilst such failures are relatively rare in production environments the consequences when they do occur can be considerable, ranging from the need for and associated cost

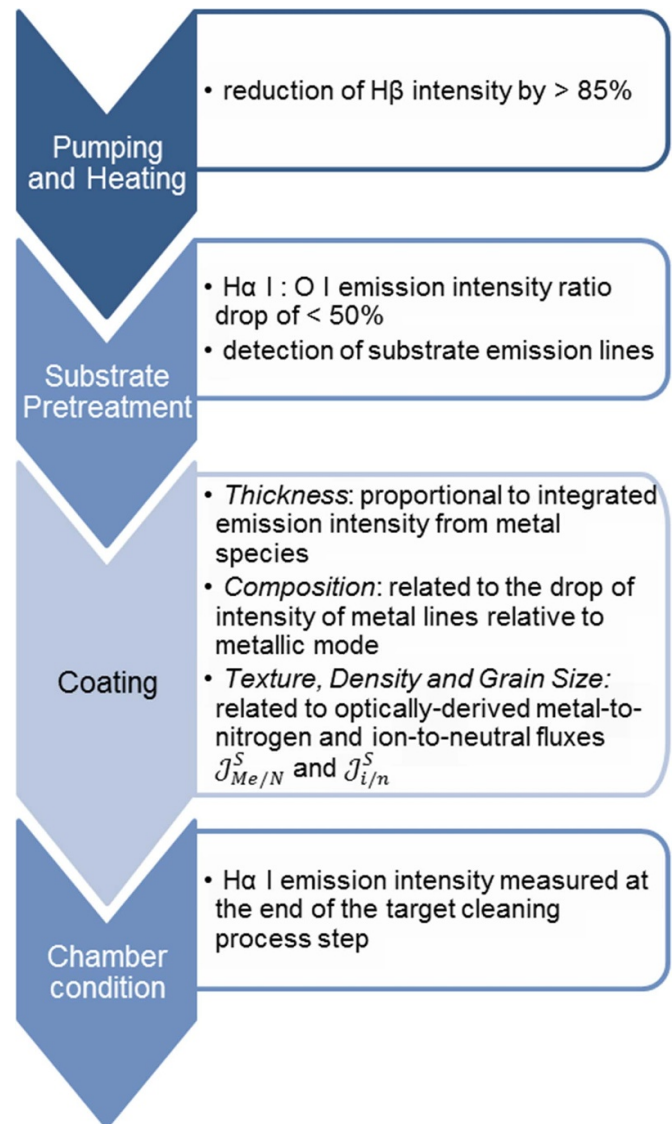


**Figure 14.** Criteria for individual process steps and chamber condition.

of reprocessing a batch to the scrapping of a complete load of high value product, hence their early detection and mitigation are critical to coating quality, equipment integrity and production potential.

The criteria established for all steps in the coating process are summarised in the flow diagram in figure 14.

### 3.7. Digital twin

The study has clearly demonstrated the versatility of OES in combination with electrical parameters for monitoring all stages of magnetron sputtering, including HIPIMS, processes and its capability to provide the primary data source for real-time digital characterization, evaluation and control of such processes and providing critical elements for a process digital twin. Unfortunately, what OES does not *a priori* provide is quantitative information about the coating being

deposited, for which empirical determination of specific parameters is required. However, as the study has shown, once these parameters have been established their combination with OES provides a powerful tool for characterizing both process and product and significantly enhances the functionality of the digital twin, potentially allowing, for example, process variability to be evaluated *in silico* rather than experimentally.

The results show that OES monitoring is significantly enhanced when combined with electrical process parameters, particularly those taking into account the diffusion of plasma from areas of strong emission towards the substrate. Dedicated physics-based analytical models utilising process data can calculate optically-derived parameters to characterise the deposition flux which are an important step in describing plasma diffusion, plasma-surface interaction, film growth and predicting coating properties. The ability to operate in real time makes physics-based models an enabling factor for digital twin. PVD processes are affected by several factors which influence the deposition environment simultaneously and whose synergistic outcome is difficult to predict. Such a multidimensional parameter space is commonly addressed through machine learning, where a number of input-output samples are observed and correlated through artificial intelligence methods. The amounts of data required can be substantially reduced by deploying physics-based models for pre-treatment which improve the accuracy of prediction whilst curbing the heuristic essence of the machine learning approach. Successful machine learning approaches have already been deployed for atmospheric pressure plasmas [44]. The physics-based models and monitoring proposed in this study can lay the basis for the introduction of artificial intelligence into a digital twin by creating a surrogate model based on physics-constrained fast classifiers which provide the appropriate grouping of OES and process data features and a means of reducing time-series data to allow mapping of features to categories (classification) practically in real time.

#### 4. Conclusions

OES in combination with external process parameters has been successfully used to monitor and optimise all stages of both HIPIMS and conventional magnetron sputtering processes. It has been shown to provide a robust method of enhancing process productivity, resource utilisation and repeatability as well as being a reliable means of process control for quality assurance purposes.

The physics-based models for the estimation of deposition flux parameters developed here are a powerful means of relating OES and process data (features) with the chemistry of the plasma and its diffusion towards the substrate. They successfully predict coating properties such as thickness, composition crystallographic orientation and morphological development during film deposition. Using suitably designed optical probes it has been possible to identify relevant emission lines for monitoring the progress of chamber evacuation, substrate/source cleaning/conditioning, and system condition-monitoring to support process optimisation and equipment utilisation. Derived from live OES and process data, the output of the models is provided in real-time and enables the operation of a digital twin of the PVD deposition process.

The physics-based models and operation boundaries identified in this research also provide a framework for the appropriate combinations of live data features for optically derived ion-to-neutral and metal-to-nitrogen flux and reduction of time series data which allows mapping of features to categories in real time and amount to a real-time digital twin. The future combination of such physics-based models with machine learning would lead to further enhancements in the precision of the feature classification models.

The work reported provides essential elements for the creation of a digital twin of the sputtering process which can be used both to monitor the process and predict outcomes such as sample surface and chamber wall contamination whilst incorporating physics-based models allowing calculation of film thickness in real time and the prediction of film texture, morphology and density. The construct allows coating design to be performed *in silico* rather than experimentally.

#### Data availability statement

The data generated and/or analysed during the current study are not publicly available for legal/ethical reasons but are available from the corresponding author on reasonable request.

#### Acknowledgment

The authors gratefully acknowledge the financial support of Innovate UK through Project (132366) Real-time Monitoring and Control of Magnetron Sputter Deposition of Thin Coatings.

## Appendix

Table A1. Optical emission lines utilised for the monitoring of the coating stages of the PVD process.

Species	Recommended monitoring step	Wavelength (nm)	Lower excitation energy (eV)	Upper excitation energy (eV)
H <sub>β</sub> I Balmer ( $n = 4 \rightarrow n' = 2$ )	Pump down and chamber condition monitoring	486.135	10.2	12.75
H <sub>α</sub> I ( $n = 3 \rightarrow n' = 2$ )	Pump down and chamber condition monitoring	656.279	10.2	12.09
OH A <sup>2</sup> Σ <sup>+</sup> – X <sup>2</sup> Π Δ <sub>v</sub> = +1	Pump down	284	—	—
OH A <sup>2</sup> Σ <sup>+</sup> – X <sup>2</sup> Π Δ <sub>v</sub> = 0	Pump down and chamber condition monitoring	309.6	—	—
O I 3p ( <sup>5</sup> P <sub>1,2,3</sub> ) – 3s ( <sup>5</sup> S <sub>2</sub> <sup>0</sup> )	Pump down, etching and chamber condition monitoring	777.194	9.15	10.74
Ar I	Etching	811.531	11.55	13.08
Fe I	Etching	348.972	0.05	3.6
Fe I	Etching	354.484	2.61	6.11
Fe I	Etching	355.826	0.99	4.477
Fe I	Etching	374.341	0.99	4.30
Fe I	Etching	422.473	3.43	6.36
Cr I 4p(z <sup>7</sup> P <sup>o</sup> )–4 s(a <sup>7</sup> S)	Coating thickness monitoring	427.481	0.00	2.899
V I 4p(y <sup>6</sup> F <sup>o</sup> )–4 s(a <sup>6</sup> D)	Coating thickness monitoring	438.471	0.28	3.11
Cr I 4p(z <sup>7</sup> P <sup>o</sup> )–4 s(a <sup>7</sup> S)	Texture monitoring	425.435	0.00	2.91
Cr I 4p(y <sup>7</sup> P <sup>o</sup> )–4 s(a <sup>7</sup> S)	Texture monitoring	359.350	0.00	3.44
Cr I 4p(w <sup>5</sup> G <sup>o</sup> )–4 s(a <sup>5</sup> G)	Texture monitoring	343.619	2.54	6.15
Ar I 4p( <sup>2</sup> [3/2])–4 s(a <sup>2</sup> [3/2] <sup>o</sup> )	Texture monitoring	810.369	11.62	13.15
N <sub>2</sub> I C <sup>3</sup> Π <sub>u</sub> – B <sup>3</sup> Π <sub>u</sub> second positive system	Texture monitoring	315.97		

## ORCID iD

A P Ehasarian  <https://orcid.org/0000-0001-6080-3946>

## References

- [1] Hovsepian P E and Ehasarian A P 2019 Six strategies to produce application tailored nanoscale multilayer structured PVD coatings by conventional and high power impulse magnetron sputtering (HIPIMS) *Thin Solid Films* **688** 137409
- [2] Klimczak A, Ozimek P and Bugyi R 2011 *Generating a Highly Ionized Plasma in a Plasma Chamber* US patent 9,840,770 B2
- [3] Bellido-González V, Daniel B, Counsell J and Monaghan D 2006 Reactive gas control of non-stable plasma conditions *Thin Solid Films* **502** 34–39
- [4] Jung J, Kim Y, Jang I Y, Kim B-G, Jeon C U, Kang M, Lee C and Hahn J W 2016 Improvement of photomask CD uniformity using spatially resolved optical emission spectroscopy *SPIE Photomask Technology (San Jose, California, United States, 2016)* vol 9985 **99851S**
- [5] Klick M 1996 Nonlinearity of the radio-frequency sheath *J. Appl. Phys.* **79** 3445–52
- [6] Stevenson J O, Ward P P, Smith M L and Markle R J 1998 A plasma process monitor/control system *Surf. Interface Anal.* **26** 124–33
- [7] Fukasawa M, Kawashima A, Kuboi N, Takagi H, Tanaka Y, Sakayori H, Oshima K, Nagahata K and Tatsumi T 2009 Prediction of fluctuations in plasma–wall interactions using an equipment engineering system *Jpn. J. Appl. Phys.* **48** 08HC01
- [8] Park S, Jeong S, Jang Y, Ryu S, Roh H J and Kim G H 2015 Enhancement of the virtual metrology performance for plasma-assisted oxide etching processes by using plasma information (PI) parameters *IEEE Trans. Semicond. Manuf.* **28** 241–6
- [9] Baek K H, Edgar T F, Song K, Choi G, Cho H K and Han C 2014 An effective procedure for sensor variable selection and utilization in plasma etching for semiconductor manufacturing *Comput. Chem. Eng.* **61** 20–29
- [10] Maggipinto M, Terzi M, Masiero C, Beghi A and Susto G A 2018 A computer vision-inspired deep learning architecture for virtual metrology modeling with 2-dimensional data *IEEE Trans. Semicond. Manuf.* **31** 376–84
- [11] Godfrey A R, Ullal S J, Braly L B, Edelberg E A, Vahedi V and Aydil E S 2001 New diagnostic method for monitoring plasma reactor walls: multiple total internal reflection Fourier transform infrared surface probe *Rev. Sci. Instrum.* **72** 3260–9
- [12] Sangiovanni D G, Edström D, Hultman L, Chirita V, Petrov I and Greene J E 2012 Dynamics of Ti, N, and TiN x (x = 1–3) ad molecule transport on TiN(001) surfaces *Phys. Rev. B* **86** 155443
- [13] Gall D, Kodambaka S, Wall M A, Petrov I and Greene J E 2003 Pathways of atomistic processes on TiN(001) and

- (111) surfaces during film growth: an *ab initio* study *J. Appl. Phys.* **93** 9086–94
- [14] Antonov V and Iordanova I 2010 Density-functional study of the crystallographic structure of chromium nitride films *J. Phys.: Conf. Ser.* **223** 012043
- [15] Barna P B and Adamik M 1998 Fundamental structure forming phenomena of polycrystalline films and the structure zone models *Thin Solid Films* **317** 27–33
- [16] Petrov I, Barna P B, Hultman L and Greene J E 2003 Microstructural evolution during film growth *J. Vac. Sci. Technol. A* **21** S117–28
- [17] Kusano E 2018 Revisitation of the structure zone model based on the investigation of the structure and properties of Ti, Zr, and Hf thin films deposited at 70–600 °C using DC magnetron sputtering *J. Vac. Sci. Technol. A* **36** 041506
- [18] Thornton J A 1977 High rate thick film growth *Annu. Rev. Mater. Sci.* **7** 239–60
- [19] Messier R, Giri A P and Roy R A 1984 Revised structure zone model for thin film physical structure *J. Vac. Sci. Technol. A* **2** 500
- [20] Ehiasarian A P, Vetushka A, Gonzalvo Y A, Sáfrán G, Székely L and Barna P B 2011 Influence of high power impulse magnetron sputtering plasma ionization on the microstructure of TiN thin films *J. Appl. Phys.* **109** 104314
- [21] Pflug A, Siemers M, Melzig T, Schäfer L and Bräuer G 2014 Simulation of linear magnetron discharges in 2D and 3D *Surf. Coat. Technol.* **260** 411–6
- [22] Music D, Geyer R W and Schneider J M 2016 Recent progress and new directions in density functional theory based design of hard coatings *Surf. Coat. Technol.* **286** 178–90
- [23] Badorreck H et al 2019 Correlation of structural and optical properties using virtual materials analysis *Opt. Express* **27** 22209
- [24] Hovsepian P E, Ehiasarian A P and Ratayski U 2009 CrAlYCN/CrCN nanoscale multilayer PVD coatings deposited by the combined high power impulse magnetron sputtering/unbalanced magnetron sputtering (HIPIMS/UBM) technology *Surf. Coat. Technol.* **203** 1237–43
- [25] Hovsepian P E, Reinhard C and Ehiasarian A P 2006 CrAlYN/CrN superlattice coatings deposited by the combined high power impulse magnetron sputtering/unbalanced magnetron sputtering technique *Surf. Coat. Technol.* **201** 4105–10
- [26] Hovsepian P E, Ehiasarian A P, Braun R, Walker J and Du H 2010 Novel CrAlYN/CrN nanoscale multilayer PVD coatings produced by the combined high power impulse magnetron sputtering/unbalanced magnetron sputtering technique for environmental protection of  $\gamma$ -TiAl alloys *Surf. Coat. Technol.* **204** 2702–8
- [27] Sáfrán G, Reinhard C, Ehiasarian A P, Barna P B, Székely L, Geszti O and Hovsepian P E 2009 Influence of the bias voltage on the structure and mechanical performance of nanoscale multilayer CrAlYN/CrN physical vapor deposition coatings *J. Vac. Sci. Technol. A* **27** 174–82
- [28] Hovsepian P E, Sugumaran A A, Purandare Y, Loch D A L and Ehiasarian A P 2014 Effect of the degree of high power impulse magnetron sputtering utilisation on the structure and properties of TiN films *Thin Solid Films* **562** 132–9
- [29] Purandare Y P, Ehiasarian A P and Hovsepian P 2016 Target poisoning during CrN deposition by mixed high power impulse magnetron sputtering and unbalanced magnetron sputtering technique *J. Vac. Sci. Technol. A* **34** 041502
- [30] Strijckmans K, Schelfhout R and Depla D 2018 Tutorial: hysteresis during the reactive magnetron sputtering process *J. Appl. Phys.* **124** 241101
- [31] Meeker D 2006 Finite element method magnetics (FEMM) femm 4.0.1 (available at: [www.femm.info](http://www.femm.info))
- [32] Schneider C A, Rasband W S and Eliceiri K W 2012 NIH Image to ImageJ: 25 years of image analysis *Nat. Methods* **9** 671–5
- [33] Puech L, Dubarry C, Ravel G and de Vito E 2010 Modeling of iron oxide deposition by reactive ion beam sputtering *J. Appl. Phys.* **107** 054908
- [34] Rossnagel S M and Saenger K L 1989 Optical emission in magnetrons: nonlinear aspects *J. Vac. Sci. Technol. A* **7** 968–71
- [35] Makino Y and Nogi K 1998 Synthesis of pseudobinary Cr-Al-N films with B1 structure by rf-assisted magnetron sputtering method *Surf. Coat. Technol.* **98** 1008–12
- [36] Hippler R, Kersten H, Schmidt M and S K H 2008 *Low Temperature Plasmas—Fundamentals, Technologies, and Techniques* vol 1 (New York: Wiley) p 119
- [37] Pintaske R, Welzel T, Schaller M, Kahl N, Hahn J and Richter F 1998 Spectroscopic studies of a magnetron sputtering discharge for boron nitride deposition *Surf. Coat. Technol.* **99** 266–73
- [38] Epstein R 1998 *Principles of Plasma Spectroscopy* ed H R Griem (Cambridge: Cambridge University Press) p 366
- [39] Wagenaars E, Bowden M D and Kroesen G M W 2005 Plasma emission imaging of a low-pressure argon breakdown *Plasma Sources Sci. Technol.* **14** 342–50
- [40] Ehiasarian A P, Andersson J and Anders A 2010 Distance-dependent plasma composition and ion energy in high power impulse magnetron sputtering *J. Phys. D: Appl. Phys.* **43** 275204
- [41] Annaloro J, Morel V, Bultel A and Omaly P 2012 Global rate coefficients for ionization and recombination of carbon, nitrogen, oxygen, and argon *Phys. Plasmas* **19** 073515
- [42] Volynets A V, Lopaev D V, Rakhimova T V, Chukalovsky A A, Mankelevich Y A, Popov N A, Zotovich A I and Rakhimov A T 2018 N<sub>2</sub> dissociation and kinetics of N(<sup>4</sup>S) atoms in nitrogen DC glow discharge *J. Phys. D: Appl. Phys.* **51** 364002
- [43] Levaton J, Amorim J and Ricard A 2012 The local dissociation phenomenon in a nitrogen afterglow *J. Phys. D: Appl. Phys.* **45** 505203
- [44] Mesbah A and Graves D B 2019 Machine learning for modeling, diagnostics, and control of non-equilibrium plasmas *J. Phys. D: Appl. Phys.* **52** 30LT02